Available online at www.sciencedirect.com
ScienceDirect
Comput. Methods Appl. Mech. Engrg. 401 (2022) 115372
Computer methods in applied mechanics and engineering
www.elsevier.com/locate/cma

Anatomy matters: The role of the subject-specific respiratory tract on aerosol deposition — A CFD study

Jana Wedel[a,*], Paul Steinmann[a,b], Mitja Štrakl[c], Matjaž Hriberšek[c], Yan Cui[d], Jure Ravnik[c]

[a] *Institute of Applied Mechanics, Universität Erlangen-Nürnberg, Germany*
[b] *Glasgow Computational Engineering Center, University of Glasgow, United Kingdom*
[c] *Faculty of Mechanical Engineering, University of Maribor, Slovenia*
[d] *Huazhong University of Science and Technology, Wuhan, China*

Available online 28 July 2022

Abstract

The COVID-19 pandemic is one of the greatest challenges to humanity nowadays. COVID-19 virus can replicate in the host's larynx region, which is in contrast to other viruses that replicate in lungs only, i.e. SARS. This is conjectured to support a fast spread of COVID-19. However, there is sparse research in this field about quantitative comparison of virus load in the larynx for varying susceptible individuals. In this regard the lung geometry itself could influence the risk of reproducing more pathogens and consequently exhaling more virus. Disadvantageously, there are only sparse lung geometries available. To still be able to investigate realistic geometrical deviations we employ three different digital replicas of human airways up to the 7th level of bifurcation, representing two realistic lungs (male and female) as well as a more simplified experimental model. Our aim is to investigate the influence of breathing scenarios on aerosol deposition in anatomically different, realistic human airways. In this context, we employ three levels of cardiovascular activity as well as reported experimental particle size distributions by means of Computational Fluid Dynamics (CFD) with special focus on the larynx region to enable new insights into the local virus loads in human respiratory tracts. In addition, the influence of more realistic boundary conditions is investigated by performing transient simulations of a complete respiratory cycle in the upper lung regions of the considered respiratory models, focusing in particular on deposition in the oral cavity, the laryngeal region, and trachea, while simplifying the tracheobronchial tree. The aerosol deposition is modeled via OpenFOAM® by employing an Euler-Lagrangian frame including steady and unsteady Reynolds Averaged Navier–Stokes (RANS) resolved turbulent flow using the k-ω-SST and k-ω-SST DES turbulence models. We observed that the respiratory geometry altered the local deposition patterns, especially in the laryngeal region. Despite the larynx region, the effects of varying flow rate for the airway geometries considered were found to be similar in the majority of respiratory tract regions. For all particle size distributions considered, localized particle accumulation occurred in the larynx of all considered lung models, which were more pronounced for larger particle size distributions. Moreover, it was found, that employing transient simulations instead of steady-state analysis, the overall particle deposition pattern is maintained, however with a stronger intensity in the transient cases.

Keywords: SARS-CoV-2; Aerosol; CFD; OpenFOAM

* Corresponding author.
E-mail address: jana.wedel@fau.de (J. Wedel).

https://doi.org/10.1016/j.cma.2022.115372
0045-7825/© 2022 Published by Elsevier B.V.

1. Introduction

The human respiratory tract is constantly exposed to environmental particles, as we can inhale more than 100 million particles daily, [1]. In certain cases, this is desirable for example when drugs are administered in the form of aerosols. On the other hand, inhalation of harmful particles such as exhaust residues, asbestos fibers, or viruses trapped in aerosols is undesirable. Exposure to airborne particles from various sources has been a health concern for many years, for example, inhalation of cigarette smoke or asbestos fibers, [2]. Nevertheless, the recent COVID-19 pandemic has generated additional interest in the scientific community to further investigate the spread of exhaled aerosolized particles as well as their deposition in the human respiratory tract. By January 7, 2022, the global cumulative number of confirmed SARS-CoV-2 infections is more than 300 million. The death toll associated with the coronavirus increased to more than 5.4 million cases by that date. Since its beginnings in the end of 2019 there has been various research in this field. However, there are still some uncertainties in this field, such as the gender difference, i.e. in Germany, men had a higher risk for intensive treatment than women, [3]. Nevertheless, ongoing research in this area has helped to provide important insights into the spread of the COVID-19 pandemic, i.e. a variety of studies on geographical spread as well as host-to-host spread of the virus, to understand and limit the pandemic. In this context, it was observed that the size of infectious particles is a key factor in disease spread, [4,5]. Small droplets and aerosols with $d_p < 10$ μm are much less likely to settle and therefore can travel long distances and are able to bypass the mechanical defenses of the airways and therefore penetrate deep into the airways to the alveolar region, [6]. In contrast, larger droplets deposit mainly in the upper lung regions, [4,5,7]. For a comprehensive review of experimentally determined particle size distributions, including descriptions of methods, see Han et al. [8]. Lindsley et al. [9], found that breathing can generate more infectious material in the air over time than coughing, typically producing particles with a predominant diameter of $d_p \leq 1$ μm, [10]. Therefore, to perform a comprehensive analysis of particle deposition in the human respiratory tract, it is important to consider a realistic particle distribution as used in Wedel et al. [11]. In the onset of the disease, it has been observed that the elderly have a higher mortality rate from coronavirus infection (especially those with chronic diseases), but young people are also at risk and may suffer serious health complications or develop post-covid fibrosis, [12]. The main focus has been on the alveoli, a site where severe disease is likely to develop, [13], and the disease morbidity is high, [5,14,15]. The SARS-CoV-2 virus can bind to the angiotensin-converting enzyme 2 (ACE2) receptor and enter the host cell, which is highly represented in this region. There are cases in which lower respiratory tract infections lead to severe pneumonia, possibly resulting in respiratory distress syndrome (ARDS) and death, [14]. However, the development of typical lung disease profiles associated with the alveolar region caused by SARS-CoV-2 requires that infectious aerosols reach the lower airways. Therefore, more particles in the lower lung region are associated with a higher risk for developing a severe cause of disease. Nevertheless, the lower lung is not the only region of interest. Recently, it has been reported that the COVID-19 virus can replicate independently in the host larynx in the early stages of infection, [16,17]. The laryngeal region includes the vocal folds, which create a cross-section of flow constriction of elliptical or triangular shape, [18]. Consequently, SARS-CoV 19 differs from other viruses such as SARS that replicate exclusively in the lungs, [16]. This is thought to be a cause of the higher transmission rate of COVID-19 virus compared with other viruses, [16].

To date, several studies have been conducted on the airflow and deposition of aerosolized particles inside the human respiratory tract using *in vivo*, *in vitro*, and *in silico* approaches, [12]. However, *in vivo* studies are usually limited due to human or animal safety issues, [12].

In general, *in vitro* studies have particularly considered upper airways and simplified geometries, [1]. Several authors have presented experimental data on the deposition of particles in single bifurcation tube models, [19–21]. Olson et al. [22], using steady-state inhalation, examined flow patterns in a realistic model of the upper and central airways. Kim and Fisher, [23], provide measurements of particle deposition in a symmetric airway model with double bifurcation based on Weibel's model. Zhou and Cheng, [24], experimentally investigated the regional efficiency of particle deposition in a nine-branch replica of the human lung. In addition, Zhang and Finlay, [25], experimentally investigated the influence of cartilage rings and showed their effects on local deposition of microparticles. Lizal et al. [26], presented a positron emission tomography-based method for *in vitro* measurements of regional aerosol deposition in a model of the human tracheobronchial tree. Moreover, Lizal et al. [27] provide an excellent review of available methods for measuring single-phase and two-phase dispersed flows for lung airflow analysis and particle deposition in *in vivo* and *in vitro* applications.

In *in silico* studies usually idealized symmetric lung models as proposed by Weibel (WA), [28], are employed. In addition, Horsfield et al. [29], presented geometric data sets for asymmetric tracheobronchial trees. Kim et al. [30], numerically investigated the aerosol deposition in different lung models (excluding oral and nasal cavities) using a classical WA airway and two Kitaoka models, [31], under differing inspiratory conditions. The author showed that geometric variations alter the deposition patterns. However, the effects of varying flow rate for both models considered were found to be similar, [30]. Image technology has enabled the generation of realistic replicas of the human lung, see for example Ley et al. [32]. Nowak et al. [33], investigated the deposition between a Weibel A-type airway model and a model based on computer tomography (CT) and attributed the significant deviations in deposition pattern to the variations of geometric features. The authors found that the Weibel A-type model is generally unable to predict realistic particle deposition patterns. Longest et al. [34], compared deposition in a standard induction port and a more realistic mouth-throat (MT) model and concluded that the models should be able to conserve the irregular MT shape to produce useful deposition predictions. Kleinstreuer and Zhang, [35], investigated laminar to turbulent flow effects and differences in deposition patterns of nano and micronsized particles in a replica of the upper lung, i.e. mouth and trachea, combined with a Weibel-type bifurcation. Farkas and Balashazy, [36], evaluated the deposition behavior of particles in an asymmetric tracheobronchial model and showed that a localized deposition pattern occurs for all particle sizes, which is more pronounced for larger particles. The authors further showed that the deposition density in hotspots can exceed the average deposition fraction by a factor of hundreds or thousands.

Zhang et al. [37], evaluated microparticle deposition in a realistic replica of the human oral airway and concluded that the turbulence following the oral airway constriction increases local particle deposition in the laryngeal region. Yang et al. [38], investigated the influence of different inlet conditions on flow structures in constricted airways using four different three-generation Weibel-type models. The author showed that inlet conditions have a significant influence on the resulting airflow structures as well as mass distributions and pressure drops. In addition, Ertbruggen et al. [39], investigated the deposition of microparticle under steady inspiratory flow in an airway model based on Horsfield's morphological data. Augusto, [40], studied the influence of physical mechanisms, particle diameter, and inspiration conditions on deposition pattern of particles in a triple bifurcation model. The author showed that for lower velocity conditions, the error increases when gravitational settling and Brownian motion are neglected. The author also observed that the total deposition increases with rising Reynolds and Stokes numbers. Koullapsis et al. [41], studied particle deposition in a realistic replica of the human airway and investigated the effects of inlet conditions and electrostatic charge. Furthermore Koullapsis et al. [42], performed a benchmark study of regional aerosol deposition in the human airway and concluded that flow in the upper lung is affected by mesh size and turbulence model, but is less sensitive to inlet conditions as their impact vanish in the laryngeal region. Wedel et al. [7], studied the effect of aerosol deposition in scaled lungs and thus age groups based on Lagrangian particle tracking in turbulent flow. Particles in smaller lungs were found to be less prone to penetrate deeply into the airways, whereas older individuals were more vulnerable, [7]. In addition, Wedel et al. [11], investigated particle deposition during various levels of physical exercising in a realistic human lung replica in different room sizes. In their study, various breathing conditions, from rest to intense activity, were compared using particle distributions from realistic expiratory events, i.e. breathing, sneezing and coughing. The authors concluded that vigorous exercise should be avoided in situations with a high concentration of suspended aerosols.

In general, most researchers have assumed steady air-particle flow. However, there are fewer contributions targeting the analysis of transient airflow effects and deposition in realistic human lung replicas. Li et al. [43,44], investigated transient effects on airflow for a model with asymmetric geometry of a simplified tracheobronchial tree (including trachea) considering varying inlet conditions and airway geometry. In addition, Li et al. [1], studied particle deposition under transient inhalation conditions using typical respiration cycles and Stokes numbers. Lambert et al. [45], investigated turbulent flow in a realistic upper airway replica by employing large-eddy simulation (LES). Jayaraju et al. [46], examined the RANS $k-\omega$, detached eddy simulation (DES), and LES in a simplified MT replica and concluded that the latter two agreed well with experimental measurements. Moreover, the authors found that DES and LES significantly improved the prediction of particle deposition, especially in the case of particle diameters $d_p < 5$ μm. Si et al. [18], studied particle expiration with particular attention to the anatomy of the larngopharyngeus. The author showed that a change in laryngopharyngeal anatomy significantly affected breathing resistance and the resulting pattern of particle deposition, [18]. Recently, Wu et al. [16], numerically investigated the exhaled viral load for particles released from the larynx and lung and showed that particles originating from

the laryngeal region lead to a higher exposure dose for susceptible individuals in the vicinity of the host. Excellent reviews of the deposition of particles in the human respiratory tract using computational models have been published in [2,47–49].

In summary, the above studies clearly demonstrate the importance of the breathing scenarios considered, particle size, accurate replication of a realistic human lung, and treatment of turbulence and boundary conditions in evaluating airflow and particle deposition in the human lung. Although there are many studies using CFD methods, the comparison of particle deposition across realistic replicas of human lungs is sparse due to the limited availability of geometries. Therefore, results may be subject or gender specific, as the geometric features of the lung can significantly affect airflow and particle deposition patterns, as shown in the above studies. In addition, fixed particle sizes are often used and realistic particle size distributions, such as those produced by expiratory events like breathing, sneezing or coughing, are rarely considered. In addition, there are few studies quantitatively comparing viral load in the larynx for different realistic geometries of the human lung. Because the anatomic lung features can alter local deposition and, in particular, the larynx as a critical site for virus propagation could crucially influence the risk of a higher exhaled viral load, it is important to conduct a particle deposition study using different realistic lung geometries under varying inlet conditions with a special focus to the laryngeal region.

In this study, we assume a correlation between the number of viruses transported to each lung region and the local amount of salivary volume deposited. In addition, we conjecture a correlation between the amount of aerosolized saliva in the laryngeal region with a higher viral propagation and thus a potential higher risk of exhaling an increased viral load. We also associate an increased risk of developing severe COVID-19 disease with higher amounts of aerosols in the lower lung regions. In addition, it should be noted that this study uses three subject-specific replicas of the human respiratory tract, omitting the nasal cavity and consequently limiting the investigation to oral inhalation. Since the use of transient simulations has been demonstrated to produce higher quality results, we compare both steady-state and transient approaches in this paper.

The paper is organized as follows: In Section 2, the airway geometry considered and the particle size distributions studied are introduced. Also, Section 2 reviews the governing equations of the flow field and particle tracking. In Section 3, the frozen flow field approach together with Lagrangian particle tracking is applied to the subject-specific human lung to study the regional volumetric deposition fraction as well as local deposition hotspots at steady state inhalation. Moreover, in Section 4, a study of transient particle deposition in the female and male respiratory geometry is performed using a realistic respiratory cycle. Finally, Section 5 summarizes the work presented and highlights the main conclusions.

2. Methods

2.1. Considered airway geometries

In the present study, we employ three realistic lung replicas obtained from medical imaging, see Fig. 1. The geometry shown in Fig. 1(a, b) represents a realistic airway replica simplified for experimental purposes, see Koullapsis et al. [42], and will be referred to as experimental geometry hereafter. This experimental geometry was provided by Lizal et al. [26,42]. Lizal et al. [26], adopted this replica to conduct *in vitro* and *in silico* measurements of regional deposition ratios of di-2-ethylhexyl sebacate (DEHS) particles. In addition, Wedel et al. [7], employed this model to compare regional aerosol deposition across various age-groups. Moreover, Wedel et al. [11], employed this experimental geometry to investigate the effect of different exercise levels on particle deposition behavior. To ensure gender equality in our studies, we additionally use a subject-specific male and female lung replica, which clearly present subject-dependent anatomic features, as shown in Fig. 1(c–f). However, we do not claim that the geometric features identified for the male and female lung presented are representative of their respective genders. In addition, Fig. 1 highlights the area that includes the larynx, which was chosen for all models to contain the lung geometry after the oral cavity up to the entrance of the trachea. Note that this region, further referred to as the larynx region, may vary in size among the subject-specific lungs considered. Furthermore, Fig. 1 presents the additional sections of the lung models. It is important to point out that the bifurcations are divided such that 30 % of the parent branch is accounted to the next generation to achieve comparability between the models considered. Moreover, the female and male airways contain bifurcations up to the 9th and 10th generation, whereas the experimental lung contains bifurcations up to the 7th generation. Besides, not all bifurcations of a given level are resolved in the

presented geometries, which affects the resulting particle deposition count per level of bifurcation. Therefore, we decide to analyze the deposition up to the 7th generation and normalize the deposition to the number of bifurcations present per level. Overall, Fig. 1 shows the presence of geometric differences between the considered airway replicas. In the respiratory models examined, significant anatomical variations are observed in the shape of the oral cavity, the shape and angle of the trachea, and especially the anatomy of the larynx. Moreover, all initial geometries are equipped with an inlet pipe whose length $l_{inlet} = 10 \times D_{inlet}$ was chosen to facilitate CFD computation of a developed flow profile at the mouth. Note that the provided experimental lung has an inlet diameter of $D_{inlet} = 2$ cm, whereas the female and male lung have $D_{inlet} = 1$ cm.

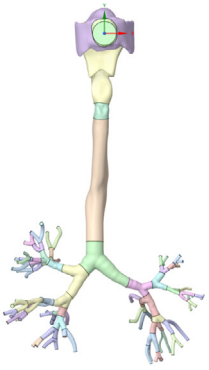

(a) experimental lung (front view) [42]

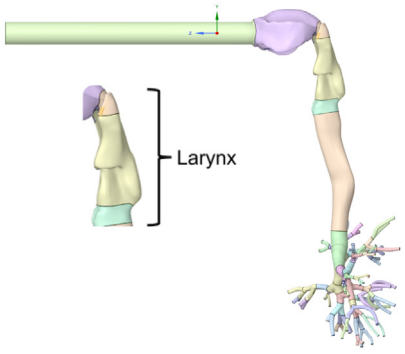

(b) experimental lung (side view) [42]

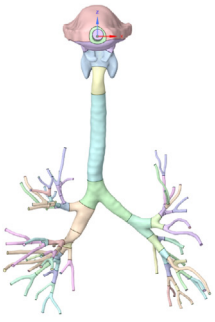

(c) female lung (front view)

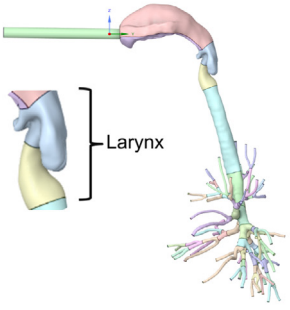

(d) female lung (side view)

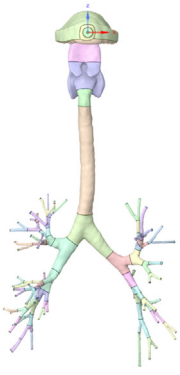

(e) male lung (front view)

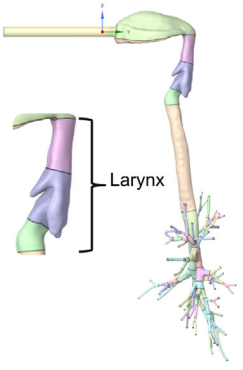

(f) male lung (side view)

Fig. 1. Comparison of the subject-specific respiratory models studied. Note that the size ratios of the different geometries are not representative, as they were modified for presentation purposes.

2.2. Pulmonary ventilation and aerosol modeling

The volume of air inspired or exhaled per minute $\dot{V}_e$ is called minute ventilation, [50]. It depends on the average respiratory rate (also called breathing rate) $\bar{f}_B$ per minute and an average tidal volume $\bar{V}_T$ as follows:

$$\dot{V}_e = \bar{f}_B \bar{V}_T \,. \tag{1}$$

The average ventilatory parameters of an adult at rest are a respiratory rate of $\bar{f}_B = 12\,\text{breaths/min}$ and a tidal volume of $\bar{V}_T = 500\,\text{ml/breath}$, giving a minute ventilation of $\dot{V}_e = 6\,\text{l/min}$, [50]. With increasing activity levels, $\dot{V}_e$ can increase up to 180 l/min, depending on exercise and individual, [50]. For a detailed analysis of the influence of different exercise levels, please see Wedel et al. [11]. In this study, we examine the following three different minute ventilations $\dot{V}_e$ ranging from low to moderate activity level, i.e. $\dot{V}_e = 7.5\,\text{l/min}$, $\dot{V}_e = 15\,\text{l/min}$, $\dot{V}_e = 30\,\text{l/min}$, [11]. In agreement with Wedel et al. [7,11], the density of the inhaled expiratory aerosol is chosen to be $\rho_p = 1,704\ \text{kg/m}^3$ as suggested by Lindsley et al. [51]. To generate reliable statistics, we inject 10^5 randomly distributed aerosol particles at the entrance of the mouth region, located at the position of the coordinate system in Fig. 1. Moreover, the particles are injected with the local flow velocity. As already described in Section 1, the behavior of aerosols is largely characterized by their size. However, exhaled particle sizes are highly dependent on the subject, health status and respiratory activity, [52,53]. In this study, we examine particle size distributions similar to those in Wedel et al. [11], see Fig. 2, which allows us to investigate a wide range of aerosol sizes, i.e. breath and cough generated droplets as well as sneeze droplet nuclei:

- Duguid [54]: Sneezing (droplet nuclei),
- Chao et al. [55]: Coughing (droplets, aerosols),
- Fabian et al. [10]: Breathing (aerosols).

Note that for all particle size distributions considered, the majority of particles are much smaller than $d_p < 10\,\mu\text{m}$. Overall, less than 0.3 % of particles studied were larger than $d_p > 100\,\mu\text{m}$. In agreement with Wedel et al. [7,11], it is assumed that the walls of the respiratory tract are covered with mucus. This is accounted for by assuming that particles adhere to the lungs once they come into contact with the internal airways, [42]. Depending on the lung ventilation considered, we adjust the time step to ensure a maximum particle Courant number of $Co_p \leq 1.0$.

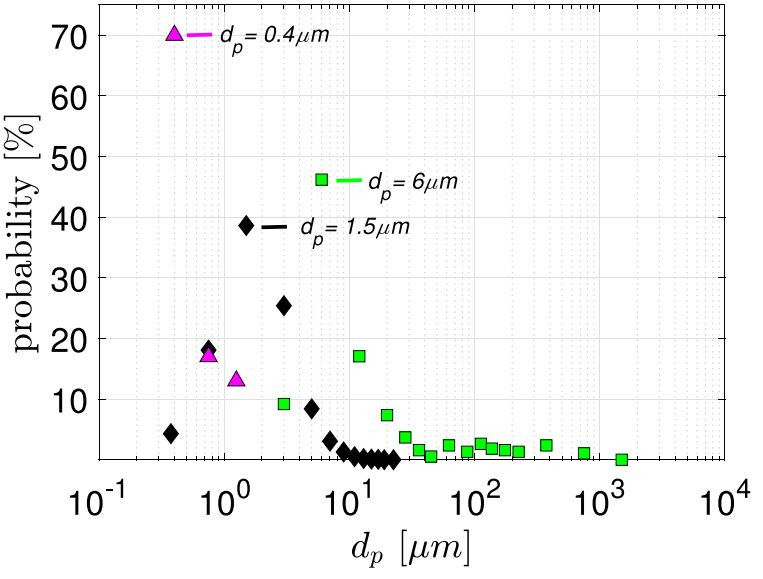

Fig. 2. Probability of expiratory aerosol and droplet sizes: ▲ breath generated droplets [10], ◆ sneeze generated droplet nuclei [54], ■ cough generated droplets [55].

2.3. Governing equations

The dispersed flows of spherical particles is modeled by employing an Euler-Lagrangian frame.

2.3.1. Flow field

The most popular approach for modeling flow in the lung is the RANS approach as it requires less computational effort, however, at the expense of accuracy, [48]. Zhang and Kleinstreuer, [56], studied the upper human airway and showed that the RANS method combined with the k-ω turbulence model generally could not adequately reproduce the results of the LES computational method, [48]. Nevertheless, the authors showed that the use of RANS with k-ω-SST in lung replicas containing only a few bifurcations lead to a good agreement with the LES method.

In this article, the flow field within the human airway is solved in an Eulerian framework. In conformity with Wedel et al. [7,11], we use the open-source software OpenFOAM®, [57,58], to solve for incompressible steady-state as well as transient flow in the lung geometries presented. The governing incompressible RANS equations are: [58]

$$\mathrm{d_t}(\rho_f \bar{\boldsymbol{u}}) + \mathrm{div}(\rho_f \bar{\boldsymbol{u}} \otimes \bar{\boldsymbol{u}} + \boldsymbol{\tau}^{\mathrm{RANS}}) = -\mathrm{grad}\,\bar{p} + \mathrm{div}\bar{\boldsymbol{\tau}} + \bar{\boldsymbol{f}}_D \tag{2}$$

and

$$\mathrm{div}\bar{\boldsymbol{u}} = 0\,. \tag{3}$$

Moreover, the Reynolds stress $\boldsymbol{\tau}^{\mathrm{RANS}}$ and the mean viscous stress $\bar{\boldsymbol{\tau}}$ are obtained by: [59]

$$\boldsymbol{\tau}^{\mathrm{RANS}} := \rho_f \boldsymbol{u}_i' \otimes \boldsymbol{u}_j' \tag{4}$$

and

$$\bar{\boldsymbol{\tau}} := \mu\,\mathrm{grad}^{\mathrm{SYM}}\bar{\boldsymbol{u}}\,. \tag{5}$$

OpenFOAM® uses the finite volume method (FVM) to discretize the above equations. In Eqs. (2)–(5) $\bar{\boldsymbol{u}}$, $\bar{p}$ and ρ_f denote the Reynolds-averaged fluid velocity components, pressure and fluid density, respectively. In addition, the $'$-sign in Eq. (4) denotes fluctuations so that the total velocity field reads $\boldsymbol{u} = \bar{\boldsymbol{u}} + \boldsymbol{u}'$. Moreover, the term $\bar{\boldsymbol{f}}_D$ captures the body forces. A closed system of equations, and thus a constitutive expression for $\boldsymbol{\tau}^{\mathrm{RANS}}$, is made possible by using either an approximate k-ω-SST or k-ω-SST DES turbulence model, [59,60]. The detached-eddy simulation (DES) is a hybrid model that uses a combination of RANS and LES approach, with the former applied in the attached boundary layers and the latter in the separated regions, [60]. The subgrid scale LES simulation is used where the grid density is sufficiently fine, i.e. where the grid spacing is much smaller than the turbulent shear layer thickness, [60]

2.3.2. Particles

In computational fluid dynamics (CFD), particle transport is usually described in either the Lagrangian or Eulerian frame, [48]. For particles with diameters $d_p > 0.3\,\mu\mathrm{m}$ the Lagrangian approach is considered appropriate, while for particles with $d_p < 0.3\,\mu\mathrm{m}$ the Eulerian approach is described as advantageous, [48]. A detailed discussion of both approaches can be found in the review articles by Rostami et al. [49], and Tang and Guo, [61].

Since our study considers particles with $d_p > 0.3\,\mu\mathrm{m}$, see Fig. 2, the Lagrangian frame is used in this article to describe the motion of the dispersed phase (aerosols, droplets), [62], which are treated as point masses. Therefore, a set of ordinary differential equations (Newton's second law) is evaluated along the particle trajectory to track the position and velocity of the particles, leading to the following equations:

$$\mathrm{D_t}\boldsymbol{x}_p := \frac{d\boldsymbol{x}_p}{dt} = \boldsymbol{u}_p, \tag{6}$$

$$\mathrm{D_t}(m_p \boldsymbol{u}_p) := m_p \frac{d\boldsymbol{u}_p}{dt} = \rho_p \frac{d_p^3 \pi}{6} \frac{d\boldsymbol{u}_p}{dt} = \sum \boldsymbol{F}_i, \tag{7}$$

where $\boldsymbol{x}_p$ is the position vector, $\boldsymbol{u}_p$ the velocity, ρ_p the density and d_p the diameter of the spherical particle. In addition, $\sum \boldsymbol{F}_i$ takes into account the sum of the forces acting on the particle, [62].

In this study, we consider aerosols and droplets produced by breathing, sneezing, and coughing, resulting in a particle size range of $0.4\ \mu\mathrm{m} \leq d_p \leq 1500\ \mu\mathrm{m}$. For particles with $d_p \geq 1\,\mu\mathrm{m}$ the drag $\boldsymbol{F}_D$, the buoyancy $\boldsymbol{F}_B$ and the gravitational force $\boldsymbol{F}_G$ predominate, simplifying Eq. (7) to: [63]

$$m_p \frac{d\boldsymbol{u}_p}{dt} = \boldsymbol{F}_D + \boldsymbol{g} V_p \left[\rho_p - \rho_f\right], \tag{8}$$

where m_p, V_p, ρ_p are the mass, volume and density of the particle. Furthermore, ρ_f denotes the fluid density and $\boldsymbol{g}$ is the gravitational acceleration. In this study we employ the standard drag force model of OpenFOAM® for spherical particles (denoted as *sphereDrag*), which is obtained as follows: [62]

$$\boldsymbol{F}_D = \frac{3}{4}\frac{\rho_f}{\rho_p}\frac{m_p}{d_p}\frac{C_d}{C_c}[\boldsymbol{u}-\boldsymbol{u}_p]|\boldsymbol{u}-\boldsymbol{u}_p|, \tag{9}$$

with the slip correction factor C_c and drag coefficient C_d:

$$C_d := \begin{cases} \frac{24}{\mathrm{Re}_p}[1+\mathrm{Re}_p^{2/3}/6]; & \mathrm{Re}_p \leq 1000\,. \\ 0.424; & \mathrm{Re}_p \geq 1000\,. \end{cases} \tag{10}$$

as well as the particle's Reynolds number

$$\mathrm{Re}_p := \rho_f d_p |\boldsymbol{u}_p - \boldsymbol{u}|/\mu\,, \tag{11}$$

which depends on the fluid density ρ_f, the relative particle-fluid velocity $|\boldsymbol{u}_p - \boldsymbol{u}|$ and the particle diameter d_p, [64]. For the considered submicron droplets $d_p < 1\,\mu$m in air, the rarefaction impact becomes apparent and a slip velocity occurs at the particle surface, which requires the consideration of a slip correction, [65]. This slip effect depends mainly on the Knudsen number $Kn = \lambda/d_p$ [65], which relates the mean free path length of the molecules λ to the particle diameter d_p. The slip velocity at the particle surface occurs when d_p is of the order of λ, [65]. In agreement with Wedel et al. [11], for modeling aerosols we use the findings of Rader, [66], who established empirical constants for oil droplets in air, leading to the following slip correction factor C_c:

$$C_c^{Rader} = 1 + 2Kn\,[1.209 + 0.441\exp[-0.779/2\,Kn\,]]\ . \tag{12}$$

In conformity with Koullapsis et al. [42], we neglect other forces such as Brownian motion, added mass, and the Basset history force, [62]. To account for the interaction of the particles with the turbulent eddies in the RANS framework, additional models are needed to approximate the fluctuation velocity. Therefore, we use the OpenFOAM® model *StochasticDispersionRAS*, [67]. In this model, a fluctuation velocity $\boldsymbol{u}'$ is calculated to perturb the velocity field in a random direction, with a Gaussian distribution with mean zero and variance σ, [42]. The above equations are implemented in a customized version of the OpenFOAM®'s solver *icoUncoupledKinematicParcelFoam*.

2.4. Limitations

The limitations of the employed set-up are consistent with those of our previous studies, [7,11]. Therefore, we initially assume a steady-state flow field alongside a dilute particle suspension. Thus, we consider a one-way coupling of particles and fluid. We also assume isotropic turbulence and the k-ω-SST RANS turbulence model. Furthermore, we employ transient simulations to mimic particle deposition during realistic respiration cycles, using both k-ω-SST and k-ω-SST DES turbulence models. Moreover, we consider sufficiently small aerosols such that their surface tension leads to small spherical rigid particles, [68]. The applicability of the RANS turbulence approach with one-way coupling in the flow and particle range considered was demonstrated in [7,11] and is therefore assumed to be equally suitable in the context of this study

3. Particle deposition in realistic human airway geometries using steady-state flows

The simplified airway model of Koullapsis et al. [42], alongside with the realistic female and male lung models employed in this study are shown in Fig. 1(b). The boundary condition used and solver information for the steady-state approach are provided in Table 1. Note that breath actually originates from the alveoli of the lungs. However, because of the varying number of branches and the lack of measured flow rates at each outlet of the realistic human lung replicas, we use a fixed flow rate at the inlet and constant pressure at the outlets of the respiratory models studied.

In addition, Table 2 presents the statistics of the generated meshes of airway models considered. The presented meshes were validated in the scope of a grid independence study.

Table 1
Computational details of considered lung model.

Flow solver:	RANS with k-ω-SST [69]
Inlet BC.:	P: zeroGradient
	U: specified flowrates
Outlet BC.:	P: fixed value
	U: zeroGradient

Table 2
Computational details of generated meshes for the considered airways.

Airway	Experimental lung	Female lung	Male lung
Cells	8.3 Mio	9.7 Mio	8.5 Mio
Boundary layers	5	5	5
Near wall distance	$y^+ \approx 1$	$y^+ \approx 1$	$y^+ \approx 1$

3.1. Flowfields

As mentioned in Section 2.2, flow rates in the range of 7.5–30 l/min are considered for all lung geometries studied, covering rest to moderate exercise. In Figs. 3 and 4 the contours of the mean velocity magnitude and turbulent kinetic energy in the central sagittal plane are compared for the three airway geometries.

It is evident that the mean velocity distribution in the throat region varies considerably due to changes in airway anatomy. However, a common feature is the presence of an acceleration region in the posterior part of the throat. The peak velocity for the female and male lungs is located in the inlet region of the mouth, whereas the peak velocity for the experimental lung is found in the trachea. The strong difference in the magnitude of the velocity in the mouth region of the investigated models is related to the larger inlet diameter (and thus the lower Reynolds number) for the experimental lung, resulting in a locally strongly reduced velocity.

In general, the velocity level in the central saggital plane is similar for female and male lung geometries despite the strong geometric differences. Nevertheless, the second acceleration region in the trachea is more pronounced in the female lung. For identical inlet Reynolds numbers $\mathrm{Re} := \rho_f D_{inlet} |\boldsymbol{u}| / \mu$, where D_{inlet} denotes the diameter of the inlet pipe, the second acceleration region of the experimental lung is of the same magnitude as in the female lung. However, in the experimental lung the high velocity region extends to the end of the trachea, while in the female lung the velocity decreases strongly toward the bifurcations. Overall, velocity in the central sagittal plane increases significantly toward higher activity levels, i.e. higher flow rates, in all airways studied.

In the next step, the turbulent kinetic energy distribution in the central sagittal plane is analyzed, see Fig. 4. It can be seen that the peak turbulent kinetic energy k_{max} is significantly higher for more intense exercises, i.e. higher flow rate, for all airway geometries. Nevertheless, the turbulent kinetic energy varies strongly with the lung geometry. Both female and male lungs have a zone of high turbulent kinetic energy in the mouth region, while k is here significantly lower in the experimental lung model. In addition, the female lung has a second region of high k in the trachea. This higher k region is also apparent in the male lung, however, with notably less intensity. In the case of the experimental lung, the high k region in the trachea is the same magnitude than for the female lung with identical Reynolds number, but slightly less extended.

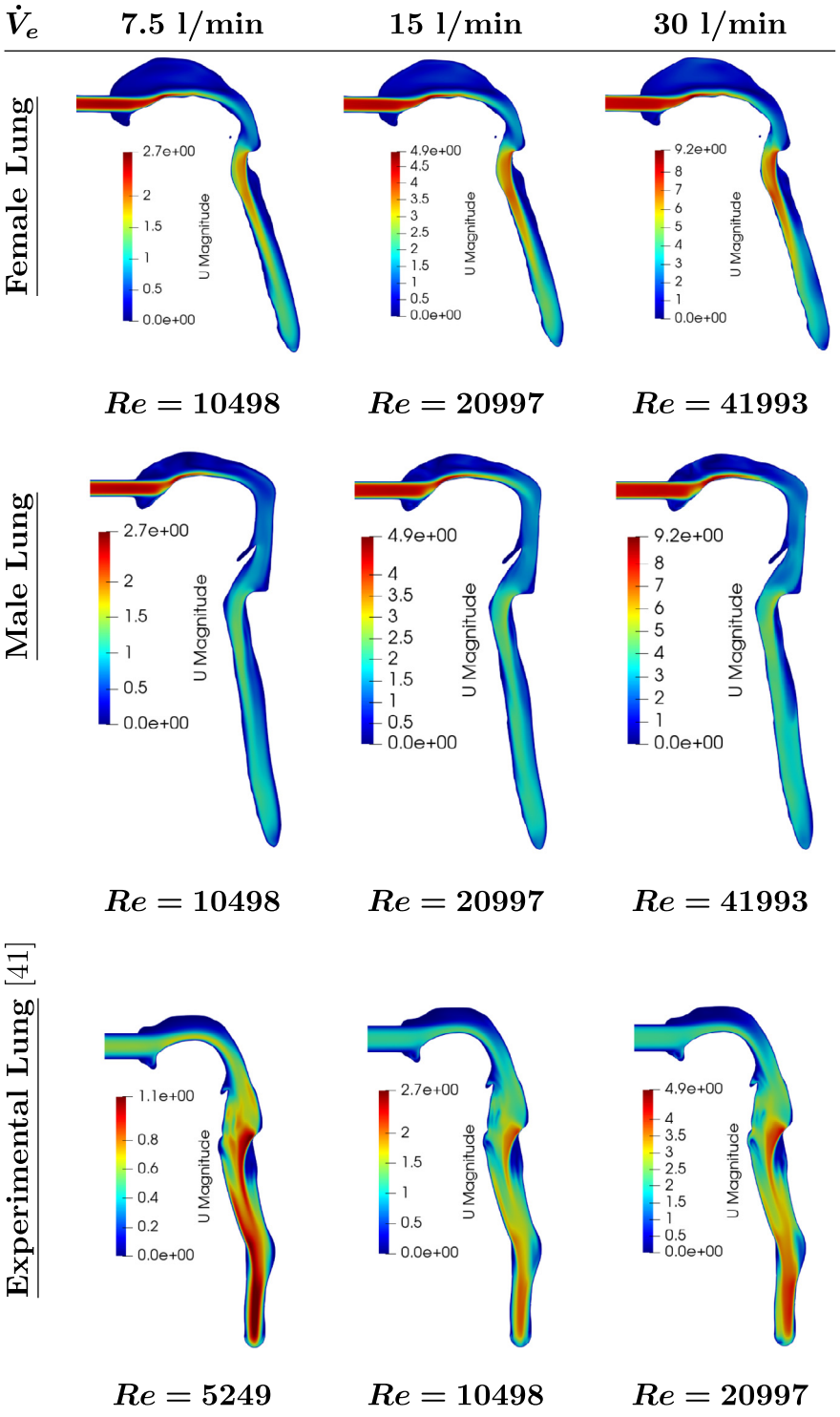

Fig. 3. Velocity magnitude profile $|\boldsymbol{u}|$ in the central sagittal plane for varying lung geometries and exercise levels. (Note the different scaling).

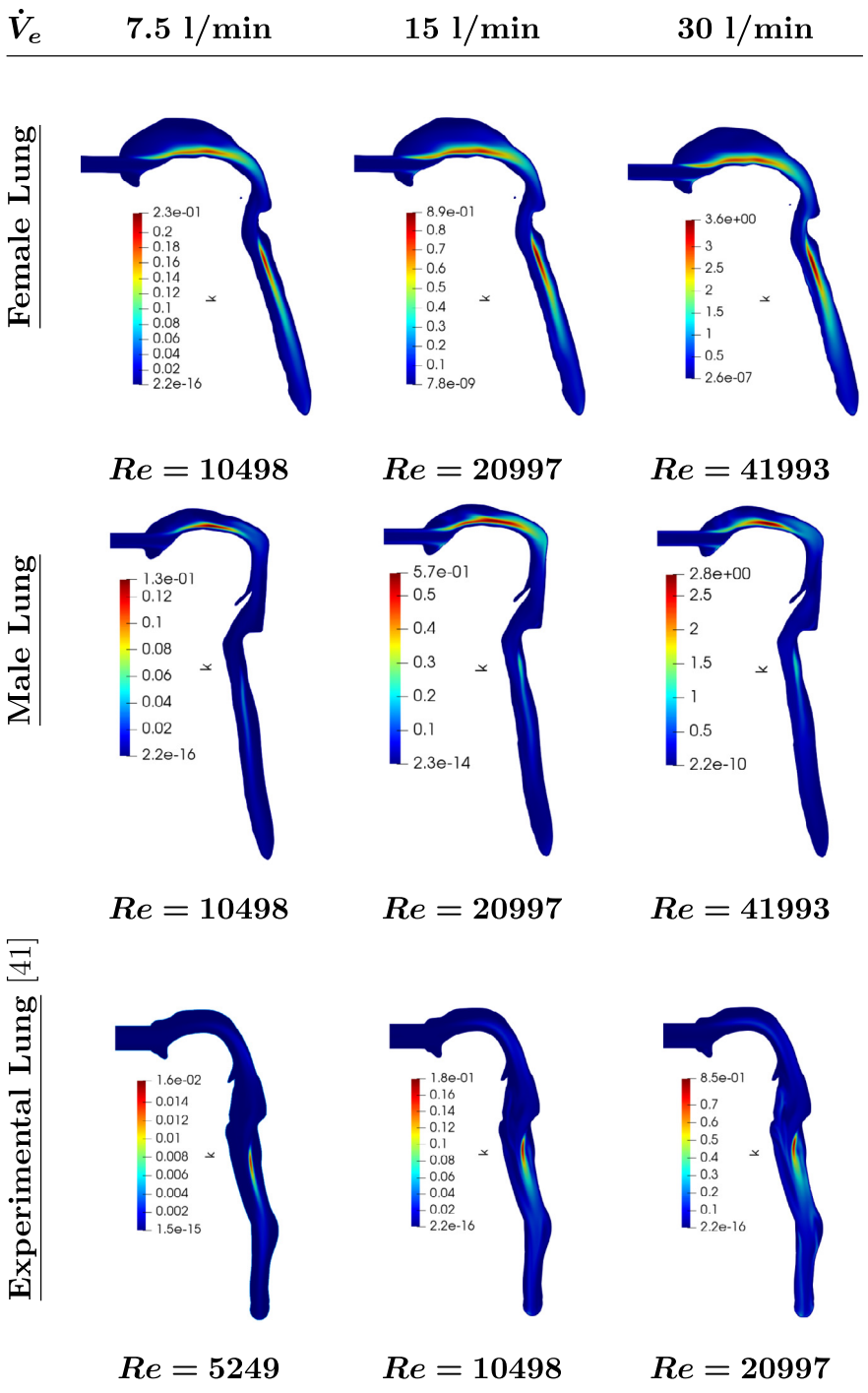

Fig. 4. Turbulent kinetic energy k in the central sagittal plane for varying lung geometries and exercise levels. (Note the different scaling).

3.2. Hydrodynamic comparability

Furthermore, we evaluate the hydrodynamic resistance of the studied airway geometries to assess whether the lungs are hydrodynamically comparable. Therefore, we calculate the hydrodynamic resistance as follows:

$$R = \frac{\Delta p}{\dot{V}_e}\,, \tag{13}$$

where Δp denotes the pressure (surface averaged) difference between airway inlet and outlet. As presented in Table 3, there is hydrodynamic comparability between the two realistic lung replicas, i.e. female and male model, with a slightly higher hydrodynamic resistance of the female lung. On the contrary, the experimental lung exhibits less than half the hydrodynamic resistance as the realistic airway geometries.

Table 3
Computational details of generated meshes for the considered airways.

Airway	Dimensions	Experimental lung	Female lung	Male lung
$\int_{A_{inlet}} p/\rho \, \mathrm{dA_{inlet}}$	[m^4/s^2]	7.47e−04	4.12e−04	3.84e−04
ρ	[kg/m^3]	1.204	1.204	1.204
A_{inlet}	[m^2]	3.14e−04	7.85e−05	7.85e−05
p_{outlet}	[Pa]	0.0	0.0	0.0
$\dot{V}_e$	[l/min]	7.5	7.5	7.5
R	[Pa s/l]	22.91	50.492	47.08

In the next step, we compare the turbulence structures in the oral cavity and larynx. A commonly used method for visualizing vortices is the Q criterion, which is used to calculate the second invariant of the velocity gradient tensor: [70]

$$Q = \frac{1}{2}\left[\left[\mathrm{tr}\,(\nabla \boldsymbol{u})^2\right] - \left[\mathrm{tr}\,(\nabla \boldsymbol{u} \cdot \nabla \boldsymbol{u})\right]\right] . \tag{14}$$

Q iso-surfaces are often used as indicators of turbulent flow structures. Fig. 5 shows the obtained Q iso-surface of $Q = 1000\,\mathrm{s}^{-2}$ in the oral cavity and laryngeal region of the airway geometries under investigation.

As presented in Fig. 5, the observed turbulent flow structures in the oral cavity vary greatly between different mouth geometries as well as activity levels. In the case of the female lung and the experimental lung, the vorticity is initially dominant in the tongue region ($\dot{V}_e = 7.5$ l/min) and intensifies toward the posterior region of the mouth. In the male geometry, the vortices are more pronounced in the anterior mouth region as well as in the upper mouth part. For all geometries, the turbulent flow structures grow strongly with increasing $\dot{V}_e$. At the same inhalation rate, the experimental lung exhibits less vortices, which is related to the lower Reynolds number. However, it is noteworthy that even at the lowest Reynolds number studied, strongly pronounced turbulent flow structures are present throughout the laryngeal region for all lung replicas.

3.3. Aerosolized volume deposition

In the following, expiratory aerosols are released randomly at the entrance of the oral cavity. The initial relative velocity is set to $\boldsymbol{u}_{\mathrm{rel}} = \boldsymbol{u} - \boldsymbol{u}_p = \boldsymbol{0}$, where $\boldsymbol{u}$ denotes the flow velocity and $\boldsymbol{u}_p$ the particle velocity. Particle tracking is performed up to 2.5 s or until all particles have been deactivated, either by deposition or by escape from the lung geometry under consideration, i.e. penetration in the deeper lung parts. Depending on where the SARS-CoV-2 agents are deposited, different symptoms may occur. It is reported that the laryngeal region is a major site for virus replication of COVID-19 pathogen in the host, which is unlikely for other viruses, e.g. SARS, which replicate in deeper lung regions, [16,17]. Therefore, we divide the respiratory tract into the following regions of interest:

- mouth region (oral cavity), laryngeal region, trachea and tracheobronchial tree (up to $LoBF \leq 7$),

where $LoBF$ denotes the considered level of the branching of the respiratory tract. As already mentioned in Section 2.1, in order to compare the different lung geometries considered, we need to take into account the different number of branches per $LoBF$. The number of resolved bifurcations per bifurcation level ($LoBF$) is shown in Table 4 for the different lung geometries. Note that the female and male airways contain branches up to the 9th and 10th generation, whereas the experimental lung contains bifurcations up to the 7th level. For comparability, we examine the deposition within the tracheobronchial tree up to $LoBF = 7$, with anything beyond this being referred to as the deep lung region. Fig. 6 sketches the labeling approach for the $LoBF$ exemplified by an airwaypath through the female tracheobronchial tree.

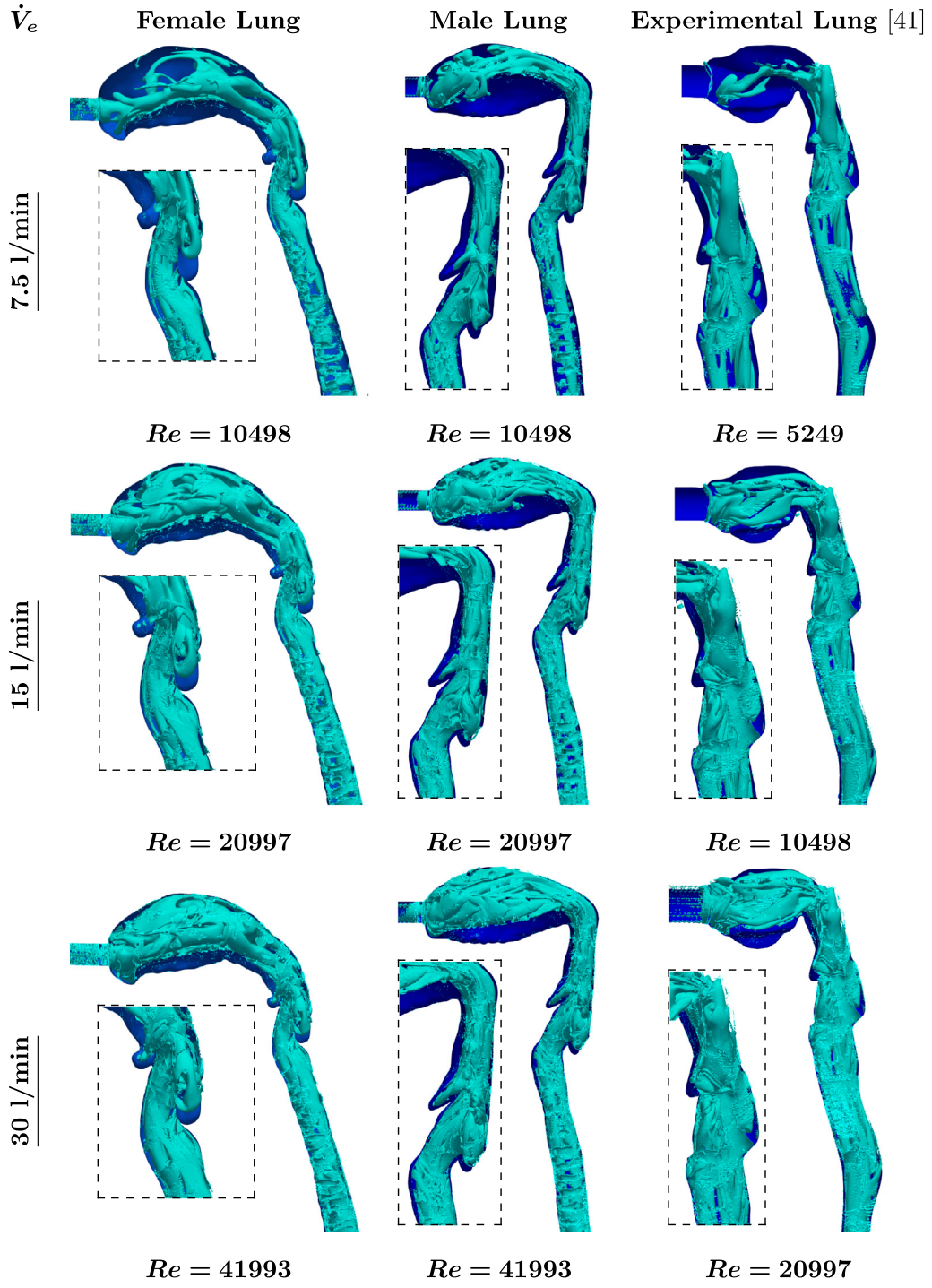

Fig. 5. $Q = 1000\,\mathrm{s}^{-2}$ isosurface for varying lung geometries and exercise level. Larynx regions are highlighted inside dotted boxes.

Table 4
Number of bifurcations per level of bifurcation (n_{BF}) for the airways considered. The level of bifurcation is denoted as $LoBF$ and n^*_{BF} labels the theoretical number of bifurcations per bifurcation level.

$LoBF$:	1	2	3	4	5	6	7
$n_{BF,Female}$	1	2	4	8	14	15	13
$n_{BF,Male}$	1	2	4	8	15	16	13
$n_{BF,Exp.}$	1	2	4	8	16	25	6
n^*_{BF}	1	2	4	8	16	32	64

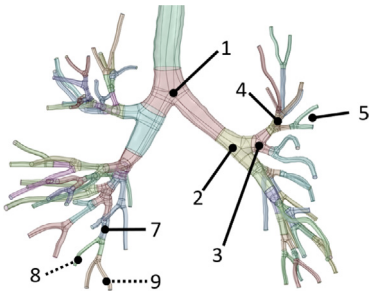

Fig. 6. Labeling of level of bifurcation exemplatory on an airwaypath of the female tracheobronchial tree.

The corrected number of deposited particles x^*_{Sim} per $LoBF$ is calculated from the deposited particles obtained by simulation, further denoted as x_{Sim}, as follows:

$$x^*_{Sim} = \frac{x_{Sim}}{n_{BF}} n^*_{BF}, \tag{15}$$

where n_{BF} is the actual number of bifurcations of a certain $LoBF$ and n^*_{BF} the corrected number of bifurcations of the specific $LoBF$, which may be written as:

$$n^*_{BF} = 2^{[LoBF-1]}. \tag{16}$$

3.3.1. Volumetric deposition

As described in Section 2.2, the inhaled particles are assumed to be generated by common exhalation activities (breathing, coughing, sneezing). Table 5 contains a detailed summary of the performed particle insertion and tracking approach.

Table 5
Computational details of particle tracking.

Time integration scheme	Implicit Euler
Forces on particles	Drag[a], gravity
Wall interaction	Touch & Stick
Cunningham correction (C_c)	Yes[b],
Turbulent dispersion	Continuous random walk
Number of particles	100000

[a]Drag coefficient (C_D) [71].
[b]Rader (1990) [66].

First, we compare the volumetric deposition fraction for 10^5 inhaled particles, i.e. particles produced by breathing, coughing, or sneezing, to obtain reliable statistics for three exercise levels for the respiratory geometries considered. Thus, the inhaled saliva masses for 10^5 particles of the studied particle size distribution render:

- Breath generated aerosols: $m_{Breath} \approx 0.033$ ng,
- Sneeze generated droplet nuclei: $m_{Sneeze} \approx 4.991$ ng,
- Cough generated droplets: $m_{Cough} \approx 536381.968$ ng

Fig. 7 displays the volumetric deposition in the four regions of interest, including the total deposition in these regions, which is denoted as overall deposition. As presented in Fig. 7, approximately 100 % of the inhaled saliva volume consisting of cough-generated particles is depositing in the oral cavity for all geometries and flow rates studied. This is due to the presence of large droplets (up to $d_p \leq 1500$ μm) in the cough droplet distribution, which carry the majority of the inhaled saliva volume and deposit almost immediately. In contrast, the deposition of breath-generated particles firstly becomes apparent in the laryngeal region and thereafter, so that almost no breath-generated particles deposit in the oral cavity. Besides, the male and experimental lung geometries filter more breath-generated particles in the upper lung, i.e. they experience a higher deposition rate in the overall geometry up to $LoBF = 7$. Consequently, these geometries potentially allow less breath-generated salivary volume to enter the deeper lung regions than the female lung. Note that due to the smaller size of breath generated droplets (0.4 μm $\leq d_p \leq$ 1.25 μm), their overall deposition efficiency is significantly lower than for the droplet nuclei generated by sneezing (0.375 μm $\leq d_p \leq$ 22.5 μm) or droplets generated by coughing (3 μm $\leq d_p \leq$ 1500 μm). In addition, Fig. 7 shows that the particle distribution of intermediate size, i.e. droplet nuclei generated by sneezing, experiences the largest variation in deposition between the lung models studied. Looking at the deposition efficiency in the oral cavity, a similar trend of increasing deposition at higher flow rates is seen in the female and male lungs. In both cases, the deposition efficiency in the oral cavity is in the range of 20 % − 40 % of inhaled saliva volume. A common deposition trend is seen in the trachea, as the deposition efficiency decreases at 15 l/min compared to lower and higher flow rates for all geometries considered. In general, a considerably small deposition fraction in the order of 0.5 − 2 % occurs in the trachea for all airway models studied. Furthermore, a comparable deposition trend is observed in the tracheobronchial tree up to $LoBF \leq 7$ for male and female lungs, with deposition increasing from 7.5–15 l/min and remaining approximately constant for 15–30 l/min with an overall deposition efficiency between 20–30 %, with a slightly higher deposition inside the female geometry. For the experimental lung, the overall deposition efficiency is always higher than 30 % and continues to increase to over 60 % for $\dot{V}_e = 30$ l/min. The most obvious difference between the considered geometries is found in the laryngeal region, where all geometries show diverging trends with increasing flow rate. While the statistic deposition fraction in the male larynx is rather unaffected by an increase in flow rate (with a slight decrease in deposition), it increases in the female and experimental lungs. Note that the deposition efficiency of the experimental lung in the larynx grows to more than twice the deposition efficiency of the female lung and five times the deposition efficiency of the male airway. Overall, it can be seen that the female and male lung have higher comparability in deposition efficiency than the experimental lung, which has a significantly higher deposition rate in lung regions up to $LoBF \leq 7$ for flow rates $\dot{V} \geq 15$ l/min, despite having half the Reynolds number.

In the next step, we perform a detailed analysis of the deposition within the tracheobronchial tree up to $LoBF \leq 7$ by considering the deposition efficiency per bifurcation level as shown in Fig. 8.

Fig. 8 displays the resulting deposition efficiency per bifurcation level as well as the total deposition in the tracheobronchial up to $LoBF = 7$. Across all flow rates and particle size distributions, the deposition efficiency is higher in the experimental lung than in either the female or male airway. The greatest variation are present for the intermediate particle size distribution (droplet nuclei produced by sneezing), where a deposition efficiency up to 30 % higher is achieved for $\dot{V} \geq 15$ l/min in the experimental lung. Besides, the deposition rates of male and female lung are comparable for all particle size distributions and flow rates. In the case of cough generated droplets as well as sneeze generated droplet nuclei the differences in salivary volume deposition are small, with female lungs showing slightly higher deposition efficiency (up to 4 %) for all flow rates. In the case of breath generated droplets, the volumetric deposition fraction across all flow rates for male and female model only begin to deviate visibly after the fourth level of bifurcation ($LoBF > 4$), with the filtration rate in the female lung being lower by up to 4 % for $\dot{V} \geq 30$ l/min.

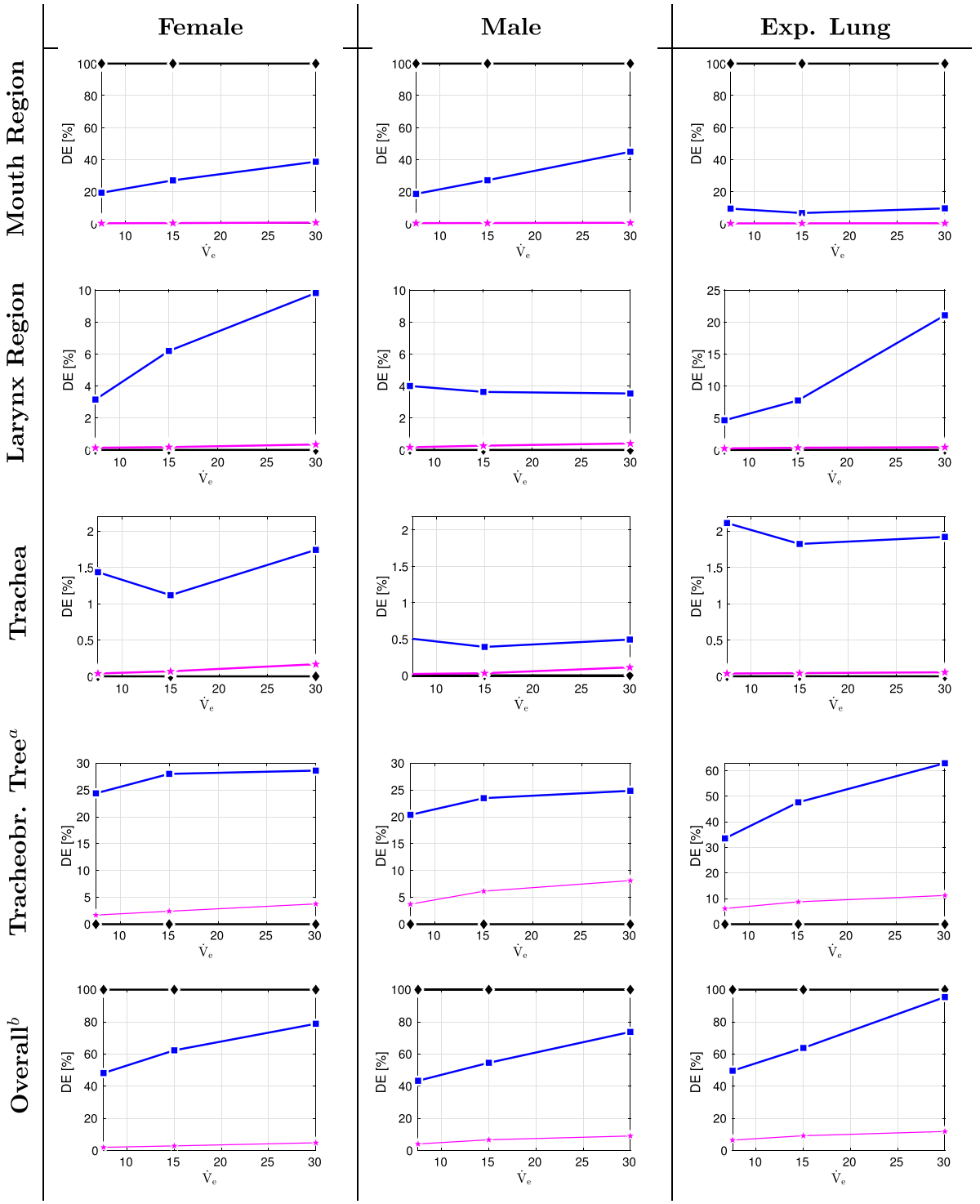

Fig. 7. Volumetric deposition fraction across three exercising levels; ◆ coughing droplets, ■ droplet nuclei of sneezing, ★ breath generated aerosols. (*a*: $LoBF = \mathbf{1-7}$, *b*: Summation of deposited particles up to $LoBF = 7$).

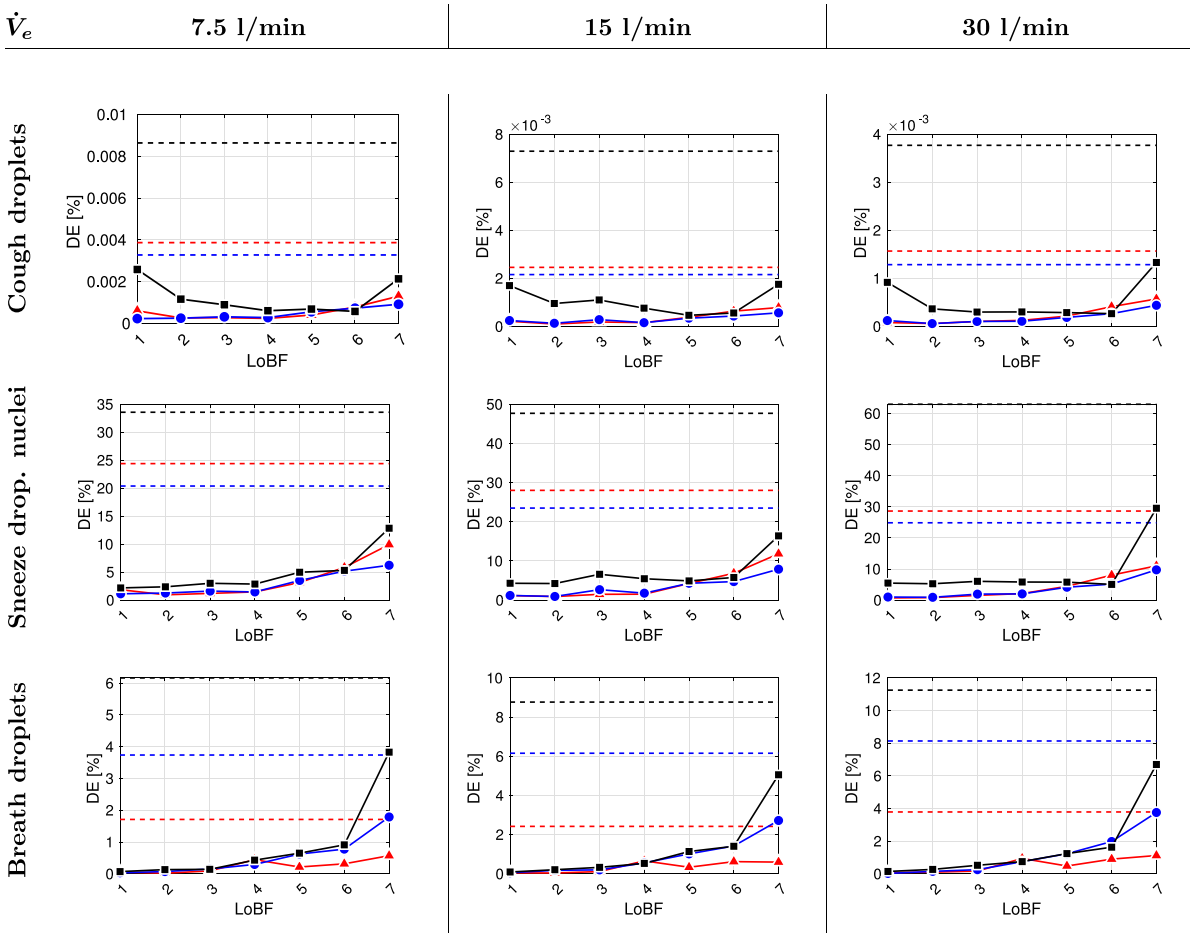

Fig. 8. Volumetric deposition fraction per level of bifurcation (LoBF) of three different particle size distributions across three exercising levels: ■ experimental lung, ▲ female lung, ● male lung. Dashed lines indicate the corresponding sum of deposition efficiencies in the tracheobronchial tree up to $LoBF$=7.

Considering both the results of the regional deposition study (shown in Fig. 7) and the detailed tracheobronchial tree analysis (shown in Fig. 8), it is highlighted that for male and female lung the deposition efficiency varies most in the laryngeal region, with a divergent deposition rate of up to 6 %. However, compared to the experimental geometry, this deviation can be considered rather small. Furthermore, we display the particles that did not deposit in the lungs regions up to $LoBF \leq 7$. Consequently, this particles can potentially penetrate to the lower lung regions, i.e. $LoBF > 7$. As shown in Fig. 9, the experimental lung has the least amount of saliva potentially entering the lower lung regions for all particle size distributions and flow rates studied. Therefore, it provides the best protection for the lower lung by achieving higher deposition in the upper lung. In addition, the filtering efficiency of the female lung for breath-generated droplets up to $LoBF \leq 7$ is lower than that of the experimental and male airways, resulting in a higher amount of inhaled saliva volume that could reach $LoBF > 7$. In contrast, of the geometries considered, the lower lung region of the male lung is most exposed to the inhaled salivary volume for larger particle size distributions, i.e. for both droplets generated by coughing and droplet nuclei generated by sneezing. Note that despite the anatomic differences in lung geometries, the regional deposition efficiencies between the female and male case are small, i.e. in the order of 5 %.

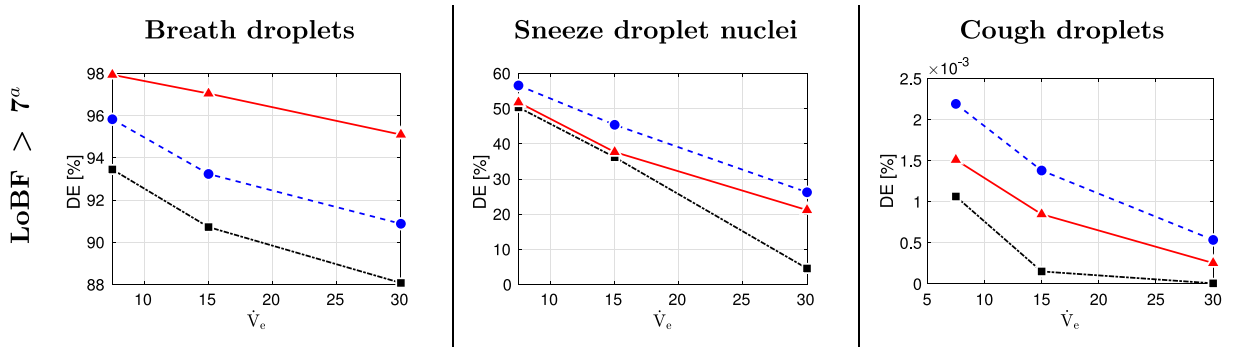

Fig. 9. Volumetric deposition fraction across three exercising levels overall and in the lower lungs: ■ experimental lung, ▲ female lung, ● male lung. (*a*: Amount of inhaled saliva volume that did not deposit in the lungs regions up to $LoBF \leq 7$ is accounted to $LoBF > 7$).

In a final step of this analysis, we evaluate the hotspots of particle deposition in the employed airway models for the moderate flow rate $\dot{V}_e = 15\,\mathrm{l/min}$. Therefore, we present the deposited particles for each particle size distribution within each lung geometry. First, Fig. 10 visualizes the hotspots of inhaled breath-generated particles. While in the male oral cavity the deposited particles are more pronounced in the anterior part of the mouth, such a trend is not evident in the female and experimental oral cavity. Moreover, in the upper lung regions, a distinct deposition hotspot is present in the folds of the laryngeal region in all geometries studied. In addition, Fig. 10, clearly shows that most particles enter the tracheobronchial trees, where deposition of breath-generated particles is higher than in the upstream regions.

In case of sneezing generated droplet nuclei, as shown in Fig. 11, a distinct particle accumulation is visible in the anterior tongue region for the female and male case. For the experimental lung, the particles are likewise more pronounced in the anterior region, however, less concentrated at a specific location. Despite the accumulation in the anterior tongue region, the proportion of deposition in the center parts of the oral cavity is smaller and the deposition is increasing toward the cavity sides. In addition to the front mouth region, clear deposition hotspots can be seen in the laryngeal region in all geometries examined, which are located in the laryngeal folds as well as in the entrance region of the trachea. In the case of female and male lung, larger particles are filtered mainly in the oral cavity as well as in the larynx and are thus less pronounced in the tracheobronchial tree. In the experimental lung, a deposition hotspot of larger particles is also visible in the first bifurcation levels. Despite an overall similar deposition fraction in the laryngeal region, as shown in Fig. 7, local particle accumulation in the larynx differs markedly between geometries.

In the case of particles produced by coughing, shown in Fig. 12, it is important to note the different scaling and coloring of the particles with $d_p > 100\,\mu\mathrm{m}$. In all geometries, these particles, which carry the majority of the inhaled saliva volume, are deposited directly in the anterior tongue area. In the case of the male and female lung, this deposition is more concentrated than in the experimental lung. Fig. 12 additionally illustrates that despite this high volumetric deposition efficiency in the oral cavity, a large number of smaller particles (with particle sizes in the range of the sneeze droplet nuclei) penetrate further into the lung. These particles produce highly pronounced deposition hotspots in the posterior region of the mouth as well as in the laryngeal folds. In the case of the experimental lung, additional particle accumulation is present in the anterior part of the trachea and extends nearly over its entire length. This pattern is less notable in the male lung. In contrast, in the female lung, particles are deposited mainly at the entrance of the trachea and no distinct deposition region is seen throughout the trachea. Similar to the droplet nuclei produced by sneezing, a strong deposition region is observed in the first two branches inside the experimental lung, which is less pronounced in the male and female lung branches.

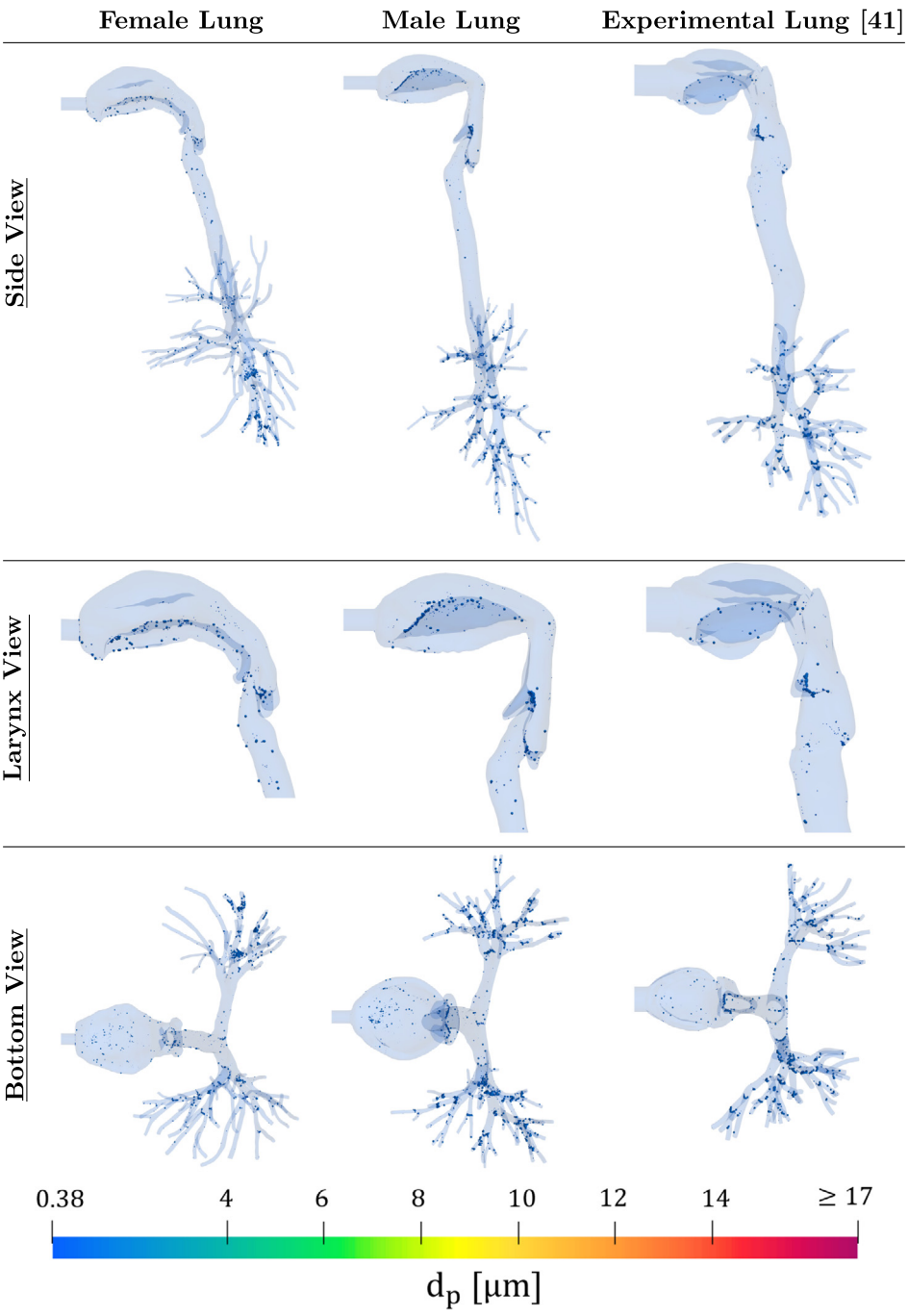

Fig. 10. Local particle deposition for $\dot{V}_e = 15\,\mathrm{l/min}$ and breath generated droplet nuclei distributions. Note that particles sizes are scaled with a factor of 1000.

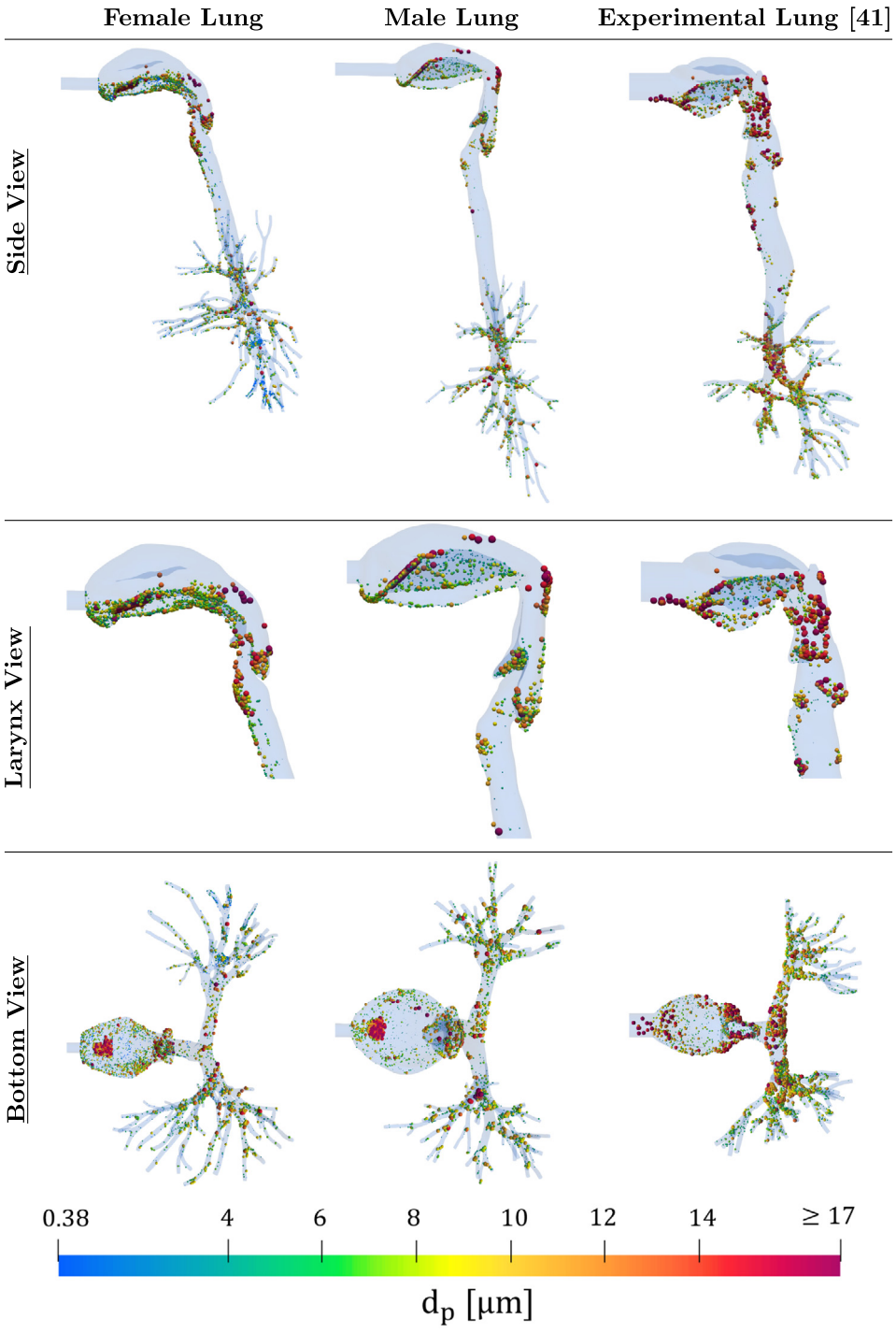

Fig. 11. Local particle deposition for $\dot{V}_e = 15$ l/min and sneeze generated droplet nuclei distributions. Note that particles sizes are scaled with a factor of 200 and highlighted in different colors. (For interpretation of the references to color in this figure legend, the reader is referred to the web version of this article.)

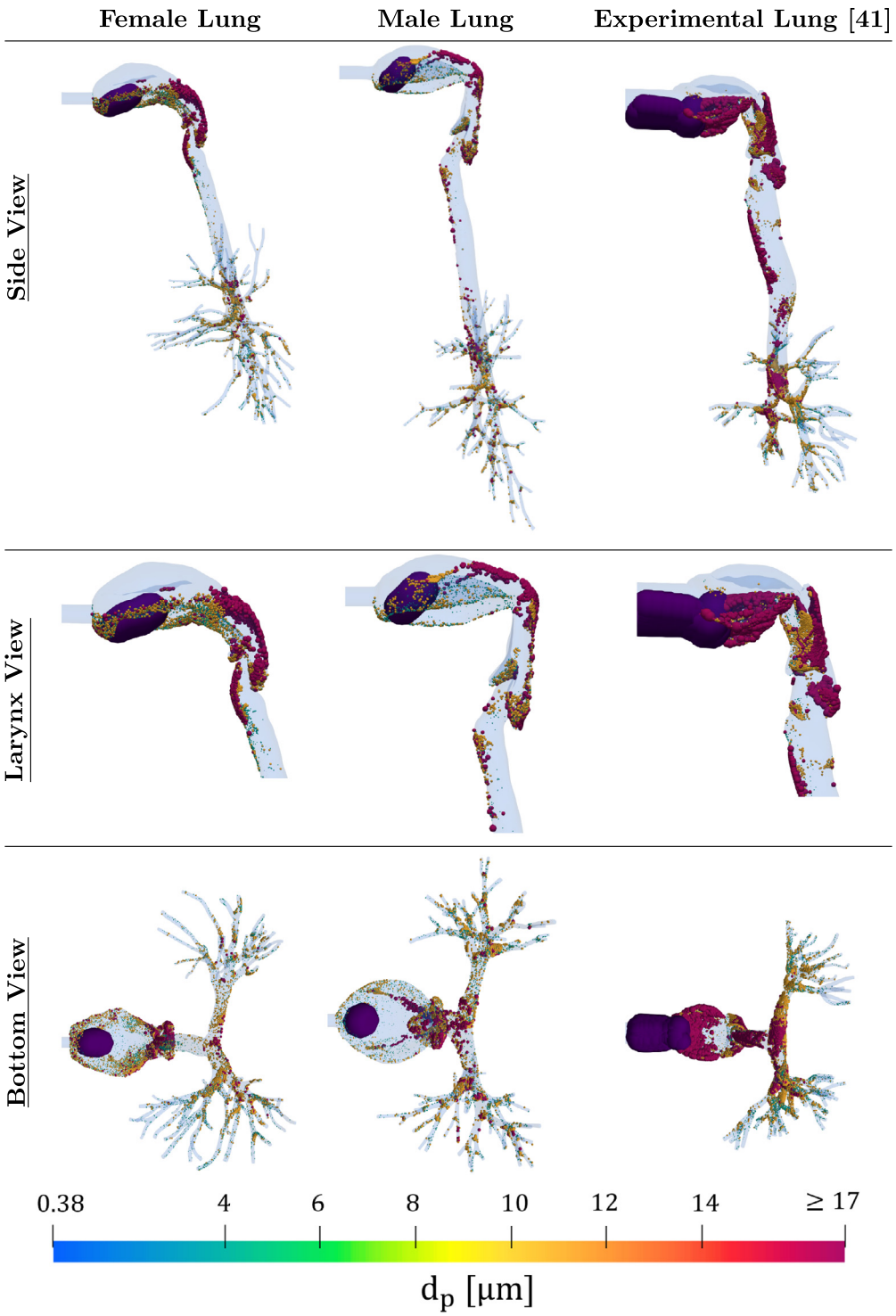

Fig. 12. Local particle deposition for $\dot{V}_e = 15\,\mathrm{l/min}$ and coughing generated droplet nuclei distributions. Note that particles sizes are scaled with a factor of 100 for $d_p \leq 100\,\mu\mathrm{m}$ and particles with $d_p > 100\,\mu\mathrm{m}$ are represented with a factor of 25 and colored in dark violet. Particles sizes are further highlighted in different colors according to the included color legend. (For interpretation of the references to color in this figure legend, the reader is referred to the web version of this article.)

3.3.2. Combined particle distribution

In this section, the results of Section 3.3.1 are employed to evaluate a combined particle size distribution of the considered expiratory events, i.e sneezing, coughing and breathing. In this regard we refer to the employed setup in [11], where a susceptible person enters the room after the symptomatic or asymptomatic host conducted a series of respiratory activities. The total volume of expelled aerosolized droplets is computed accordingly:

- 2.0×10^{-6} ml per cough, 15.0×10^{-6} ml per sneeze and 2.5×10^{-6} ml per 30 min breathing.

In the chosen scenario the symptomatic host executes the following respiratory events:

- $10\times$ coughing, $10\times$ sneezing and 90 min of breathing

This renders a overall exhaled saliva volume of 1.775×10^{-4} ml, which is assumed to be equally distributed over a specified room volume. The chosen airspace is based on bavarian school construction ordinance that specifies $6\,\mathrm{m}^3$ of air space per person. Followingly, we considered an air space of $V_{airspace} = 12\,\mathrm{m}^3$ (estimated to host 2 individuals). The duration of the exposure of the susceptible to the exhaled saliva volume is set to 90 min. Moreover, we assume a constant number of virus copies per *ml* of exhaled saliva. Viral loads are commonly measured by counting viral RNA, [72]. In the following we consider $n_{copies} = 10^8$ copies/ml, which represents a comparably high viral load found in nasopharynx samples of a symptomatic SARS-COV-2 host, see [73].

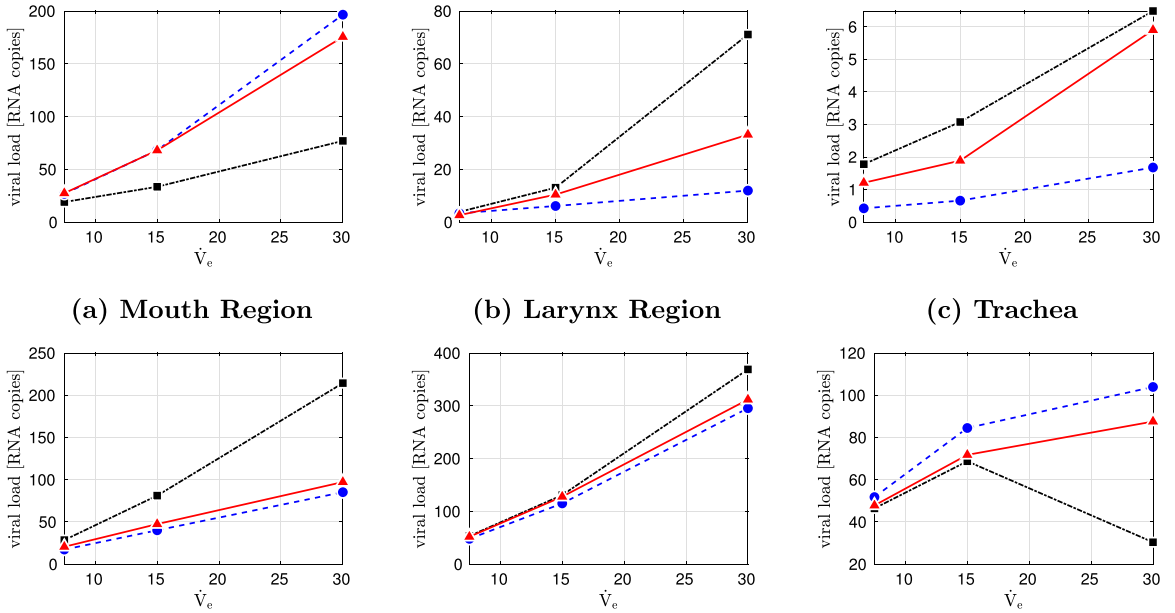

Fig. 13. Viral load (measured in RNA copies) in different lung sections: ■ experimental lung, ▲ female lung, ● male lung. (*a*: $LoBF = 1-7$, *b*: Summation of all lung regions including tracheobronchial tree up to $LoBF = 7$, *c*: Amount that did not deposit in the overall region is accounted to $LoBF{>}7$).

As shown in Fig. 13(e), the overall viral load in lung regions (up to $LoBF \leq 7$) is comparable between the subject-specific female and male lung, with a slightly higher overall deposition in the upper female airways, resulting in a lower amount of viral load potentially reaching the lower airways, see Fig. 13(e, f). Moreover, the deposition in the trachea is comparably low to the other regions of interest for all lung geometries considered. Despite the overall similar deposition trend for the realistic lung replicas, i.e. the female and male airway geometries, the distribution of RNA copies differs greatly within the geometric regions studied. The differences are particularly pronounced in the laryngeal region, see Fig. 13(b). At flow rates of $\dot{V}_e \geq 15\,\mathrm{l/min}$, viral RNA copy deposition in the female laryngeal region is approximately two to three times higher ($\dot{V}_e = 30\,\mathrm{l/min}$) than in the male counterpart. Because of the higher viral deposition in the upper lung regions, the female lung is somewhat better protected from pathogens

entering the lower airways than the male lung. However, the higher viral load in the laryngeal region may lead to higher viral reproduction and thus higher exhaled viral load.

As shown in Fig. 13(e) an overall higher viral load is present in the upper regions of the experimental lung, which is due to increased deposition in the larynx, trachea, and tracheobronchial tree up to $LoBF = 7$. Consequently, a smaller amount of virus may enter the lower lung, see Fig. 13(f). For all flow rates considered, the significantly higher deposition of viral RNA copies in the tracheobronchial tree up to $LoBF = 7$ and the larynx region in the experimental lung mainly contributes to the better protection of the lower respiratory system compared with the female and male airways especially for higher flowrates ($\dot{V}_e = 30\,\mathrm{l/min}$). Note that for $\dot{V}_e = 30\,\mathrm{l/min}$ the experimental laryngeal region experiences more than twice the viral load of the female larynx and more than six times the viral load of the male larynx, which is a consequence of reduced filtering in the oral region. Again, this could be attributed to a potentially higher risk of exhaling a greater amount of viral RNA copies in the cause of the disease.

4. Realistic respiratory cycle

So far, we have considered inspiration as a steady-state event by using the average flow rate as described in Section 2.2. To obtain a more realistic comparison, we examine the nonstationary nature of the inhalation process below. A nondimensional flow pattern of a single respiratory cycle is reconstructed based on transient flow rate measurements of a realistic human respiration, see Nishi et al. [74], recorded at a constant minute ventilation of $\dot{V}_e = 7.5\,\mathrm{l/min}$. Five respiratory cycles are recorded and averaged to obtain a representative flow pattern of a single respiratory cycle. In addition, the flow pattern is corrected by scaling the inhalation and exhalation phases equally so that the exchanged volume remains the same. To determine the actual flow patterns, we assume that the tidal volume V_T remains constant for the minute ventilations considered. Therefore, one could choose the respiration rates $\bar{f}_B = 15$, $\bar{f}_B = 30$, and $\bar{f}_B = 60$ $breaths/minute$ for the simulated average minute ventilations $\dot{V}_e = 7.5\,\mathrm{l/min}$, $\dot{V}_e = 15\,\mathrm{l/min}$, and $\dot{V}_e = 30\,\mathrm{l/min}$, respectively. The obtained flow patterns are shown in Fig. 14(a). They are generated by scaling the inhalation phase of a representative respiratory flow pattern so that the total inhaled volume corresponds to $V_T = 500\,\mathrm{ml/breath}$. We also construct the transient particle injection pattern, as shown in Fig. 14(b), by assuming a linear dependence on flow rate. As exemplarily presented for three flow rates, see Fig. 14, the transient injection rate is scaled so that the total number of 10^5 particles is injected within each inhalation cycle. In the scope of this study we will focus on the intermediate flowrate of $\dot{V}_e = 15\,\mathrm{l/min}$.

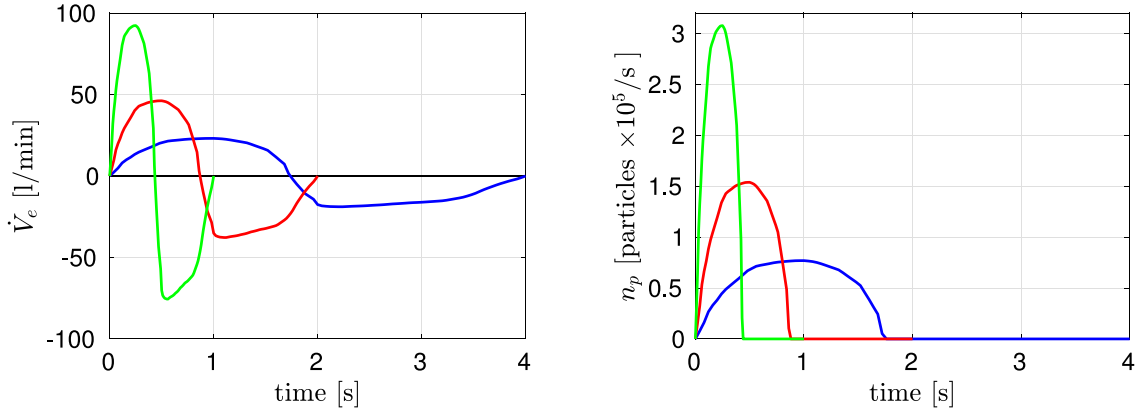

(a) breathing cycles (b) particle injection

Fig. 14. Inspiration cycles and particle injection for three different average flowrates: $\dot{V}_e = 30\,\mathrm{l/min}$, $\dot{V}_e = 15\,\mathrm{l/min}$, $\dot{V}_e = 7.5\,\mathrm{l/min}$.

Furthermore, we study the influence of two different turbulence models, namely the k-ω-SST as well as the k-ω-SST DES model, [60].

4.1. Simplified geometry

The main region of interest in this study is the influence of transient flow on viral load in the laryngeal region of a realistic human lung replica. Therefore, we simplify the female and male geometry shown in Fig. 1, while we preserve the realistic geometry of the upper lung up to the second branching level, see Fig. 15. Note that the mesh density in the remaining domain is similar to the previous mesh.

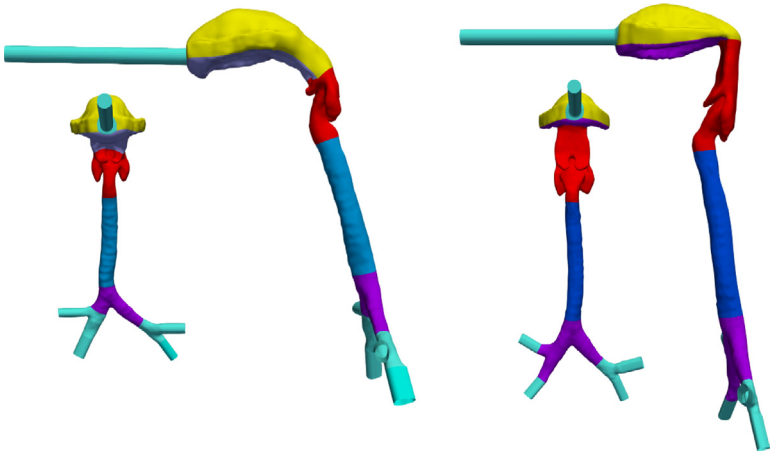

Fig. 15. Simplified female and male lung replicas. Note that the size scaling between male and female has been adjusted for visualization.

4.2. Flow field

To generate realistic breathing conditions, the flow field is initialized by simulating a complete respiration cycle with the k-ω-SST model. Fig. 16 shows the initial distribution of velocity and turbulent kinetic energy in the central sagittal plane of the studied airway replicas. As shown in Fig. 16, there is an area of increased velocity in both the oral cavity and larynx of the female and male lung model. In addition, an increase in turbulent kinetic energy is observed at the inlet of the oral cavity and larynx of both lung geometries, with slightly higher intensity in the female lung.

In the next step, we evaluate the resulting velocity distribution at the approximate time of peak inspiration ($t_{sim} = 0.5\,\mathrm{s}$) and peak expiration ($t_{sim} = 1.0\,\mathrm{s}$). The resulting velocity distribution in the central sagittal plane in the female and male lung is shown in Fig. 17. Similar to the steady-state inhalation performed, see Fig. 3, both turbulence models in the female lung at peak inspiration yield high velocity regions at the entrance of the oral cavity and at the end of the larynx that extend into the trachea. These acceleration regions are also present in the male lung, however, with a less intense second acceleration region. For both subject specific male and female airway, the differences between the k-ω-SST and the k-ω-SST DES flow field are already apparent in the oral cavity, where more vortices are present in the upper and posterior regions of the mouth when the latter model is used. In addition, k-ω-SST DES generates stronger eddies in the larynx and trachea, with the vortices in the trachea being more pronounced in the female lung considered. During peak expiration, the high velocity regions in the male and female lungs shift to the inlet tube and laryngeal region, again being less pronounced in the male geometry. Similar to peak inspiration, the use of k-ω- SST DES in peak expiration for male and female airways results in stronger fluctuations in the posterior mouth and laryngeal regions compared to the k-ω-SST model.

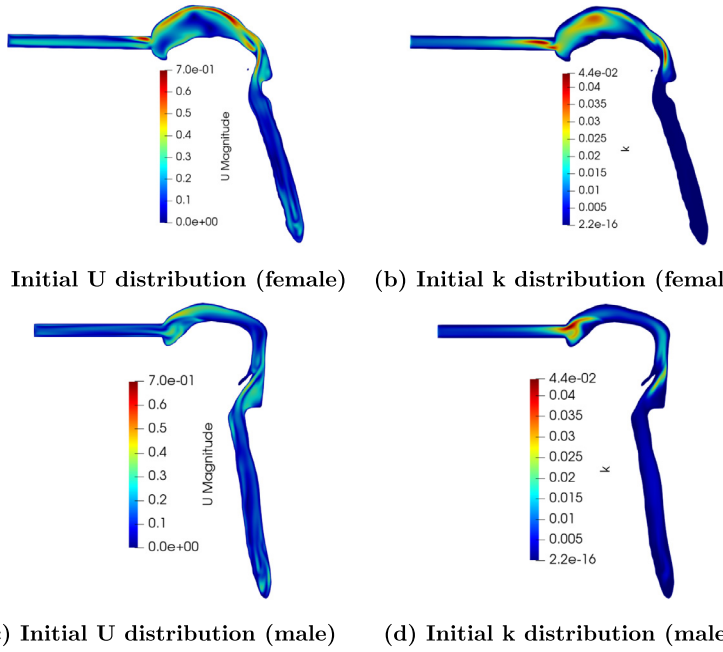

(a) Initial U distribution (female) (b) Initial k distribution (female)

(c) Initial U distribution (male) (d) Initial k distribution (male)

Fig. 16. Velocity U and turbulent kinetic energy k after one inhalation cycle in the central sagittal plane of the female and male lung replicas. Flow rate: $\dot{V} = 15\,\mathrm{l/min}$.

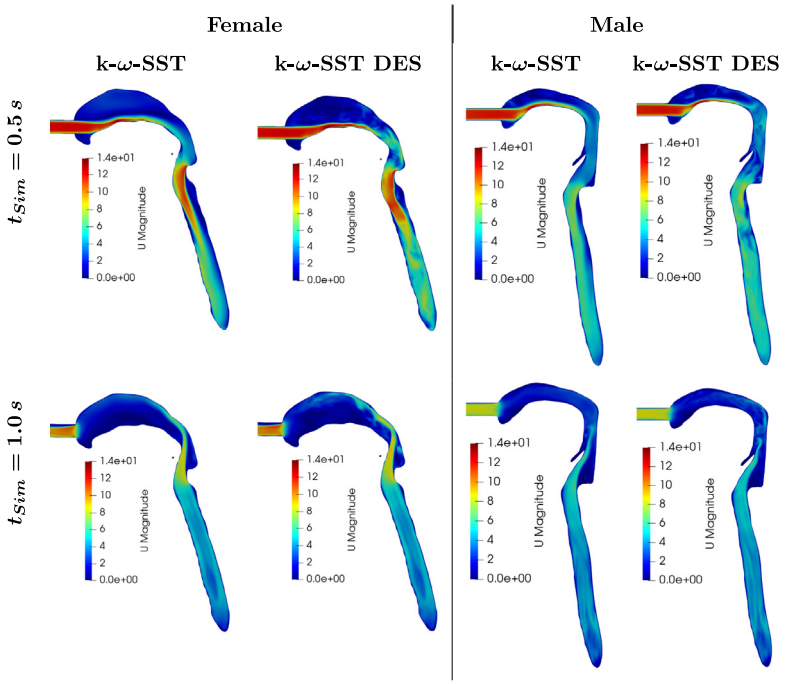

Fig. 17. Velocity U at peak inhalation ($t_{Sim} = 0.5\,\mathrm{s}$) and peak exhalation ($t_{Sim} = 1.0\,\mathrm{s}$) in the central sagittal plane of the female and male lung replicas using transient simulation with k-ω-SST and k-ω-SST DES turbulence model. Flowrate: $\dot{V}_e = 15\,\mathrm{l/min}$.

4.3. Deposition analysis

In the next step, we investigate the resulting deposition patterns obtained in the transient simulations. Fig. 18 provides a comparison of the volumetric deposition efficiencies of the simulations performed for the female and male lung for the transient simulation, where the influence of two different turbulence models is investigated, as well as for the steady-state results. Note that the transient deposition efficiency is evaluated at the end of the inhalation. As shown in Fig. 18(a), the resulting deposition fractions vary strongly with the chosen simulation approach. In the female lung, considering a transient simulation with the k-ω-SST turbulence model results in an overall 10 % larger deposition, whereas using the k-ω-SST DES model results in an increase of more than 20 %. In both cases, the increased volume fraction in the oral region is responsible for the overall higher deposition and, consequently, less saliva penetrates into the regions thereafter. Moreover, the deposition efficiency in the larynx is strongly reduced in the transient simulations compared to the steady-state analysis, to about $2-3$ %. In the case of the male lung, a similar trend is obtained, however, the deviations between k-ω-SST and k-ω-SST DES deposition results are less pronounced. As in the case of the female larynx, the deposition efficiency in the male laryngeal region is also greatly reduced in the transient simulations compared to the steady-state approach, to about 0.5 %.

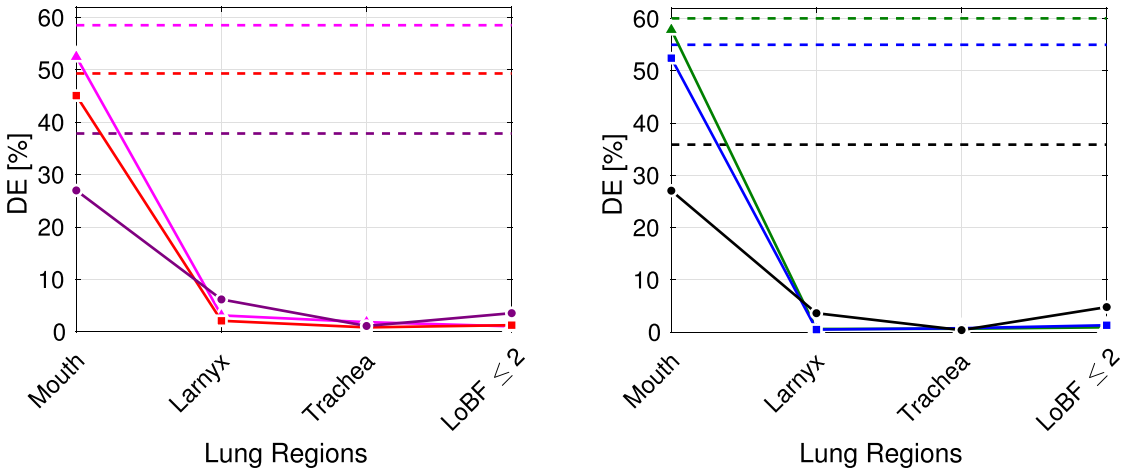

(a) Deposition Efficiency in the female lung **(b)** Deposition Efficiency in the male lung

Fig. 18. Volumetric deposition efficiency for sneeze generated droplet nuclei and $\dot{V}_e = 15\,\mathrm{l/min}$ in the female and male lung: ▲ Female lung (transient with k-ω-SST DES), ■ Female lung (transient with k-ω-SST), ● Female lung (steady-state) ▲ Male lung (transient with k-ω-SST DES), ■ Male lung (transient with k-ω-SST), ● Male lung (steady-state). Dashed lines indicate the corresponding overall deposition efficiency. (For interpretation of the references to color in this figure legend, the reader is referred to the web version of this article.)

Fig. 19 visualizes the hotspots of deposition by showing local particle accumulation within the female lung. As indicated, the deposition pattern remain similar in all simulations performed. However, the use of transient simulations increases the intensity of the hotspots in the oral cavity and larynx, with the highest increase obtained when using the k-ω- SST DES model. Moreover, in both transient simulations, there is an additional particle hotspot in the center of the posterior part of the oral cavity resulting from resolving vortices in this region, see Fig. 17. In addition, Fig. 19 shows that the k-ω- SST DES approach results in a higher deposition within the trachea compared with the other approaches, which is again due to the higher resolution of the vortices in this region, as presented in Fig. 17. The lower particle deposition in the mouth and larynx region found in the steady-state simulation could be attributed to an inadequacy of the turbulent dispersion model used.

In addition, Fig. 20 visualizes the local particle accumulations within the male lung geometry. As shown, the deposition hotspots remain similar for all simulation configurations considered. Similar to the deposition trend in the female lung, the use of a transient simulation results in more pronounced particle accumulation in the oral cavity and larynx, while maintaining a comparable deposition pattern overall. The highest deposition rate in the oral cavity is obtained by using the transient simulation in combination with the k-ω-SST DES model, while the lowest particle deposition in the upper lung is obtained in the steady-state analysis.

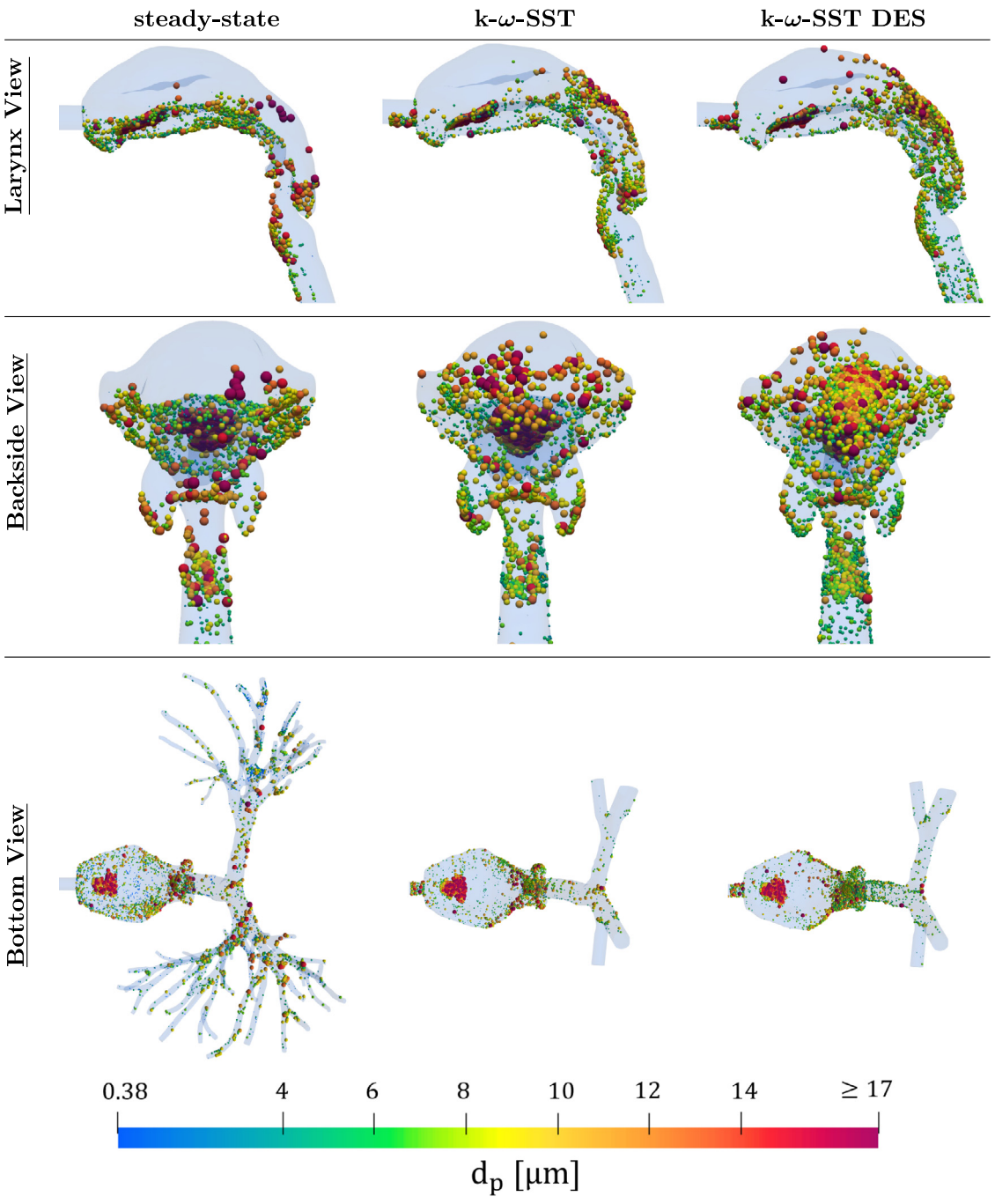

Fig. 19. Local particle deposition of sneeze generated droplet nuclei after a full inhalation for $\dot{V}_e = 15\,l/min$ inside the female lung. Note that particles sizes are scaled with a factor of 200 and highlighted in different colors. (For interpretation of the references to color in this figure legend, the reader is referred to the web version of this article.)

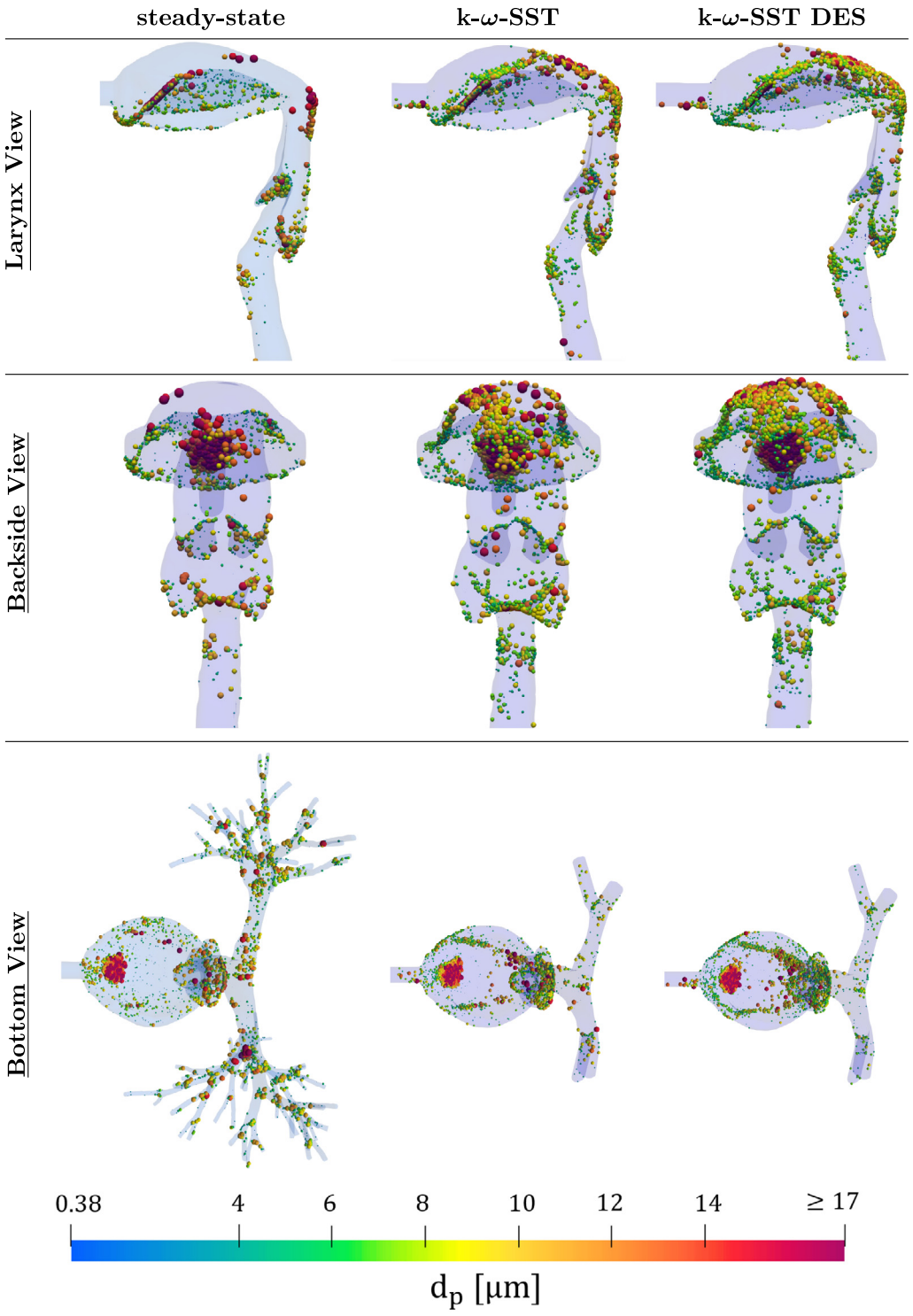

Fig. 20. Local particle deposition of sneeze generated droplet nuclei after a full inhalation for $\dot{V}_e = 15$l/min inside the male lung. Note that particles sizes are scaled with a factor of 200 and highlighted in different colors. (For interpretation of the references to color in this figure legend, the reader is referred to the web version of this article.)

5. Conclusions

In this study, we employed OpenFOAM® to gain new insights into aerosol deposition in the human respiratory tract by using three different realistic, subject-specific replicas of the human lung. In this context, we investigated different levels of inhalation ranging from rest to moderate level of exercise, i.e. 7.5 l/min, 15 l/min and 30 l/min. In addition, realistic particle size distributions generated by coughing, sneezing and breathing were considered. In the first part of our analysis, we employed a frozen flow approach in the same way as in Wedel et al. [7,11], where the computational model is based on the RANS equations with the k-ω-SST turbulence model. This model in combination with Lagrangian particle tracking has been successfully compared with the *in vitro* and *in silico* results of Koullapsis et al. [42], and is therefore considered suitable for aerosol deposition studies in the selected human airways. In the second part of our study, we investigate a realistic breathing cycle using transient simulation with two different turbulence models, i.e. k-ω-SST and k-ω- SST DES.

In the following we summarize our main findings:

- We found a large variability in regional aerosol deposition between the considered respiratory models, which we attributed to the variations in geometric lung features. This demonstrates the importance of an accurate representation of the human respiratory system to derive reliable deposition trends.
- In addition, we showed that variations in lung anatomy can significantly affect respiratory resistance, with hydrodynamic resistance in female and male lungs being approximately twice as high as in the experimental lung used.
- In agreement with Wedel et al. [7,11], we associate higher viral concentrations in the deep lung regions, a major site of COVID-19 morbidity, with a higher risk of developing severe disease profiles of the alveolar regions such as pneumonia. In this context, the experimental lung geometry provides the best mechanical protection for the lower airways, which we associate with a lower likelihood of developing a severe COVID-19 cause, as the lowest viral load is observed in the deep lung regions for all flow rates and particle size distributions studied.
- Moreover, we investigated local hotspots of aerosol deposition. In this context, particle accumulations for the subject-specific female and male lung replicas were broadly comparable for all particle size distributions considered. We also found that the effects of varying flow rate were similar in most regions of the employed lung models. Nevertheless, the effect of flow rate differed, particularly in the laryngeal region, and proved to be highly subject-specific. While statistical deposition efficiency in the male larynx was almost unaffected by flow rate, the female and experimental lungs exhibited higher deposition rates with increasing flow rate. We also found localized deposition hotspots in the laryngeal region for all particle sizes, which were more pronounced for larger particle size distributions, i.e. sneezing and coughing.
- When we considered a realistic scenario in which we employed a combination of particle size distributions and rising aerosol uptake with higher flow rate, an increase in viral load in the larynx was observed for all flow rates and for all airways considered. However, the rate of growth differed greatly between the lung geometries investigated. For example, approximately twice as many viral RNA copies were found in the experimental lung geometry as in the female lung and six times as many viral RNA copies as in the male lung.
- We associate higher salivary volume deposition in the laryngeal region with a higher risk of viral replication and, as a possible consequence, with a higher exposure dose for susceptible individuals in the vicinity of the host. Therefore, despite having the best protection of the lower lung regions, the experimental lung geometry could potentially replicate more virus in the laryngeal region due to the higher initial larynx viral load.
- In addition, we found that the use of transient simulations did not result in a significant shift in local particle deposition. Rather, the hotspots observed in the steady-state simulations proved to be more pronounced in the lung geometries studied for both transient simulations considered, while the overall deposition patterns remained comparable. We attribute the lower deposition efficiency obtained in the steady-state simulations to an inadequacy of the turbulent dispersion model used.
- The highest deposition efficiency was observed for the unsteady simulation combined with the k-ω-SST DES turbulence model, which can be attributed to a better resolution of the vortices. Thus, more particles were filtered in the oral cavity, resulting in a lower aerosol load that propagated to the regions thereafter.

Declaration of competing interest

The authors declare that they have no known competing financial interests or personal relationships that could have appeared to influence the work reported in this paper.

Data availability

Data will be made available on request.

Acknowledgments

The authors thank the Deutsche Forschungsgemeinschaft, Germany for the financial support in the framework of the project STE 544/58-2 and the Slovenian Research Agency and the Ministry of Science and Technology of China for the support of the bilateral research project BI-CN/20-22-002.

References

[1] Z. Li, C. Kleinstreuer, Z. Zhang, Particle deposition in the human tracheobronchial airways due to transient inspiratory flow patterns, J. Aerosol Sci. 38 (2007) 625–644, http://dx.doi.org/10.1016/j.jaerosci.2007.03.010.

[2] C. Kleinstreuer, Y. Feng, Computational analysis of non-spherical particle transport and deposition in shear flow with application to lung aerosol dynamics—A review, J. Biomech. Eng. 135 (2013) 021008, http://dx.doi.org/10.1115/1.4023236.

[3] U. Koppe, H. Wilking, T. Harder, et al., COVID-19-patientinnen und -patienten in deutschland: Expositionsrisiken und assoziierte faktoren für Hospitalisierungen und schwere Krankheitsverläufe, Bundesgesundheitsbl. 64 (2021) 1107–1115.

[4] I.M. Ciuca, Transmission of COVID-19 virus by droplets and aerosols: A critical review on the unresolved dichotomy, Elsevier Public Health Emerg. Collection 188 (2020) 188–109819.

[5] R.J. Thomas, Particle size and pathogenicity in the respiratory tract, Int. J. Surg. 4 (2013) 847–858.

[6] W.G. Lindsley, et al., A cough aerosol simulator for the study of disease transmission by human cough-generated aerosols, Aerosol Sci. Technol. 47 (2013) 937–944, URL https://pubmed.ncbi.nlm.nih.gov/26500387/.

[7] J. Wedel, M. Štrakl, P. Steinmann, M. Hriberšek, J. Ravnik, Can CFD establish a connection to a milder COVID-19 disease in younger people? Comput. Mech. 67 (2021) 1497–1513, http://dx.doi.org/10.1007/s00466-021-01988-5.

[8] Z.Y. Han, W.G. Weng, Q. Huang, Characterizations of particle size distribution of the droplets exhaled by sneeze, J. R. Soc. 10 (2013) URL https://royalsocietypublishing.org/doi/10.1098/rsif.2013.0560.

[9] W.G. Lindsley, et al., Viable influenza a virus in airborne particles expelled during coughs versus exhalations. Influenza and other respiratory, Viruses 10 (2016) 404–413, URL https://onlinelibrary.wiley.com/doi/10.1111/irv.12390.

[10] P. Fabian, J.J. McDevitt, W.H. DeHaan, R.O.P. Fung, B.J. Cowling, K.H. Chan, G.M. Leung, D.K. Milton, Influenza virus in human exhaled breath: An observational study, PLoS ONE 3 (2008) e2691.

[11] J. Wedel, P. Steinmann, M. Štrakl, M. Hriberšek, J. Ravnik, Risk assessment of infection by airborne droplets and aerosols at different levels of cardiovascular activity, Arch. Comput. Methods Eng. 28 (6) (2021) 4297–4316, http://dx.doi.org/10.1007/s11831-021-09613-7.

[12] D. Ciloglu, Numerical simulation of the unsteady flow field in the human pulmonary acinus, Sādhanā 46 (2021) 186, http://dx.doi.org/10.1007/s12046-021-01704-2.

[13] M. Ortiz, Heterogeneous expression of the SARS-coronavirus-2 receptor ACE2 in the human respiratory tract, EBioMedicine 60 (2020) URL https://www.thelancet.com/journals/ebiom/article/PIIS2352-3964(20)30352-2/fulltext.

[14] B.G. Madas, P. Füri, A. Farkas, et al., Deposition distribution of the new coronavirus (SARS–CoV–2) in the human airways upon exposure to cough–generated droplets and aerosol particles, Sci. Rep. 10 (2020) 22430, http://dx.doi.org/10.1038/s41598-020-79985-6, URL https://www.nature.com/articles/s41598-020-79985-6#citeas.

[15] C.W.M. Pan, J.A. Lednicky, C.-Y. Wu, Collection, particle sizing and detection of airborne viruses, J. Appl. Microbil. 127 (6) (2019) 1596–1611, URL https://sfamjournals.onlinelibrary.wiley.com/doi/full/10.1111/jam.14278.

[16] J. Wu, W. Weng, COVID-19 virus released from larynx might cause a higher exposure dose in indoor environment, Environ. Res. 199 (2021) http://dx.doi.org/10.1016/j.envres.2021.111361.

[17] R. Wölfel, V. Cormann, W. Guggemos, et al., Virological assessment of hospitalized patients with COVID-2019, Nature 581 (7809) (2020) 465–469, http://dx.doi.org/10.1038/s41586-020-2196-x.

[18] X. Si, J. Xi, J. Kim, Effect of laryngopharyngeal anatomy on expiratory airflow and submicrometer particle deposition in human extrathoracic airways, Open J. Fluid Dyn. 03 (2013) 286–301, http://dx.doi.org/10.4236/ojfd.2013.34036.

[19] J. Johnston, K. Isles, D. Muir, Inertial deposition of particles in human branching airways, Inhaled Part 04 (1975) 61–73.

[20] C.S. Kim, A.J. Iglesias, Deposition of inhaled particles in bifurcating airway models: I. inspiratory deposition, J. Aerosol Med.-Deposition Clearance Effects Lung 2 (1989) 15–27.

[21] C.S. Kim, D.M. Fisher, D.J. Lutz, T.R. Gerrity, Particle deposition in bifurcating airway models with varying airway geometry, J. Aerosol Sci. 25 (3) (1994) 567–581, http://dx.doi.org/10.1016/0021-8502(94)90072-8, URL https://www.sciencedirect.com/science/article/pii/0021850294900728.

[22] D.E. Olson, M.F. Sudlow, K. Horsfield, G.F. Filley, Convective patterns of flow during inspiration, Arch. Intern. Med. 131 1 (1973) 51–7.

[23] C. Kim, D. Fisher, Deposition characteristics of aerosol particles in sequentially bifurcating airway models, Aerosol Sci. Technol. 31 (1999) 198–220, http://dx.doi.org/10.1080/027868299304255.
[24] Y. Zhou, Y. Cheng, Particle deposition in a cast of human tracheobronchial airways, Aerosol Sci. Technol. 39 (2005) 492–500, http://dx.doi.org/10.1080/027868291001385.
[25] Y. Zhang, W. Finlay, Measurement of the effect of cartilaginous rings on particle deposition in a proximal lung bifurcation model, Aerosol Sci. Technol. 39 (2005) 394–399, http://dx.doi.org/10.1080/027868290945785.
[26] F. Lizal, M. Belka, J. Adam, J. Jedelsky, A method for in vitro regional aerosol deposition measurement in a model of the human tracheobronchial tree by the positron emission tomography, Proc. IMechE Part H: J. Eng. Med. 229 (10) (2015) 750–757, http://dx.doi.org/10.1177/0954411915600005.
[27] F. Lizal, J. Jedelsky, K. Morgan, K. Bauer, J. Llop, U. Cossío, S. Kassinos, S. Verbanck, J. Ruiz-Cabello, A. Santos, E. Koch, C. Schnabel, Experimental methods for flow and aerosol measurements in human airways and their replicas, Eur. J. Pharm. Sci. 113 (2017) http://dx.doi.org/10.1016/j.ejps.2017.08.021.
[28] E.R. Weibel, Morphometry of the Human Lung, Academic Press, Berlin, 1963.
[29] K. Horsfield, G. Dart, D.E. Olson, G.F. Fille, G. Cumming, Models of the human bronchial tree, J. Appl. Physiol. 2 (1971) 207–217, http://dx.doi.org/10.1152/jappl.1971.31.2.207.
[30] Y. Kim, Z. Tong, H. Chan, R. Yang, CFD modelling of air and particle flows in different airway models, J. Aerosol Sci. 134 (2019) 14–28, http://dx.doi.org/10.1016/j.jaerosci.2019.04.015, URL https://www.sciencedirect.com/science/article/pii/S0021850218301435.
[31] H. Kitaoka, S. Koc, S. Tetsumoto, S. Koumo, H. Hirata, T. Kijima, 4D model generator of the human lung, "Lung4Cer", in: Conference Proceedings : Annual International Conference of the IEEE Engineering in Medicine and Biology Society. IEEE Engineering in Medicine and Biology Society. Conference, Vol. 2013, 2013, pp. 453–456, http://dx.doi.org/10.1109/EMBC.2013.6609534.
[32] S. Ley, D. Mayer, B. Brook, E. Beek, C. Heussel, D. Rinck, R. Hose, K. Markstaller, H.-U. Kauczor, Radiological imaging as the basis for a simulation software of ventilation in the tracheo-bronchial tree, Eur. Radiol. 12 (2002) 2218–2228, http://dx.doi.org/10.1007/s00330-002-1391-5.
[33] N. Nowak, P. Kakade, A. Annapragada, Computational fluid dynamics simulation of airflow and aerosol deposition in human lungs, Ann. Biomed. Eng. 31 (2003) 374–390, http://dx.doi.org/10.1114/1.1560632.
[34] P. Longest, M. Hindle, S. Das Choudhuri, J. Xi, Comparison of ambient and spray aerosol deposition in a standard induction port and more realistic mouth–throat geometry, J. Aerosol Sci. 39 (2008) 572–591, http://dx.doi.org/10.1016/j.jaerosci.2008.03.008.
[35] C. Kleinstreuer, Z. Zhang, Laminar-to-turbulent fluid-particle flows in a human airway model, Int. J. Multiph. Flow. 29 (2) (2003) 271–289, http://dx.doi.org/10.1016/S0301-9322(02)00131-3, URL https://www.sciencedirect.com/science/article/pii/S0301932202001313.
[36] A. Farkas, I. Balásházy, Quantification of particle deposition in asymmetrical tracheobronchial model geometry, Comput. Biol. Med. 38 (2008) 508–518, http://dx.doi.org/10.1016/j.compbiomed.2008.01.014.
[37] Z. Zhang, C. Kleinstreuer, C. Kim, Micro-particle transport and deposition in a human oral airway model, J. Aerosol Sci. 33 (2002) 1635–1652, http://dx.doi.org/10.1016/S0021-8502(02)00122-2.
[38] X.L. Yang, Y. Liu, R. So, J. Yang, The effect of inlet velocity profile on the bifurcation COPD airway flow, Comput. Biol. Med. 36 (2006) 181–194, http://dx.doi.org/10.1016/j.compbiomed.2004.11.002.
[39] C. Ertbruggen, C. Hirsch, M. Paiva, Anatomically based three-dimensional model of airways to simulate flow and particle transport using computational fluid dynamics, J. Appl. Physiol. (Bethesda, Md. : 1985) 98 (2005) 970–980, http://dx.doi.org/10.1152/japplphysiol.00795.2004.
[40] G.L. L.L.X. Augusto, CFD evaluation of the influence of physical mechanisms, particle size, and breathing condition on the deposition of particulates in a triple bifurcation airway, Water Air Soil Pollut. 227 (2016) http://dx.doi.org/10.1007/s11270-016-2753-y.
[41] P.G. Koullapis, S.C. Kassinos, M.P. Bivolarova, A.K. Melikov, Particle deposition in a realistic geometry of the human conducting airways: Effects of inlet velocity profile, inhalation flowrate and electrostatic charge, J. Biomech. 49 (11) (2016) 2201–2212, http://dx.doi.org/10.1016/j.jbiomech.2015.11.029.
[42] P.G. Koullapis, S.C. Kassinos, J. Muela, C. Perez-segarra, J. Rigola, O. Lehmkuhl, Y. Cui, M. Sommerfeld, J. Elcner, M. Jicha, I. Saveljic, N. Filipovic, F. Lizal, L. Nicolaou, Regional aerosol deposition in the human airways : The SimInhale benchmark case and a critical assessment of in silico methods, Eur. J. Pharm. Sci. 113 (2017) 1–18, http://dx.doi.org/10.1016/j.ejps.2017.09.003.
[43] Z. Li, C. Kleinstreuer, Z. Zhang, Simulation of airflow fields and microparticle deposition in realistic human lung airway models. Part I: Airflow patterns, Eur. J. Mech. B/Fluids 26 (2007) 632, http://dx.doi.org/10.1016/j.euromechflu.2007.02.003.
[44] Z. Li, C. Kleinstreuer, Z. Zhang, Simulation of airflow fields and microparticle deposition in realistic human lung airway models. Part II: Particle transport and deposition, Eur. J. Mech. B/Fluids 26 (2007) 650–668, http://dx.doi.org/10.1016/j.euromechflu.2007.02.004.
[45] A. Lambert, P. O'Shaughnessy, M. Tawhai, E. Hoffman, C.-L. Lin, Regional deposition of particles in an image-based airway model: Large-eddy simulation and left-right lung ventilation asymmetry, Aerosol Sci. Technol. : J. Am. Assoc. Aerosol Res. 45 (2011) 11–25, http://dx.doi.org/10.1080/02786826.2010.517578.
[46] S. Jayaraju, M. Brouns, C. Lacor, B. Belkassem, S. Verbanck, Large eddy and detached eddy simulations of fluid flow and particle deposition in a human mouth–throat, J. Aerosol Sci. 39 (2008) 862–875, http://dx.doi.org/10.1016/j.jaerosci.2008.06.002.
[47] W.A. Rahim, W.M. Faizal, N.N.N. Ghazali, C.Y. Khor, I. Badruddin, M. Zainon, A. Yazid, N. Ibrahim, R. Razi, Computational fluid dynamics modelling of human upper airway: A review, Comput. Methods Programs Biomed. 196 (2020) 105627, http://dx.doi.org/10.1016/j.cmpb.2020.105627.
[48] V.K.H. Bui, J.-Y. Moon, M. Chae, P. Duck-Shin, L. Young-Chul, Prediction of aerosol deposition in the human respiratory tract via computational models: A review with recent updates, 2020, p. 137.
[49] A. Rostami, Computational modeling of aerosol deposition in respiratory tract: A review, Inhal. Toxicol. 21 (2009) 262–290, http://dx.doi.org/10.1080/08958370802448987.

[50] M. Kent, The Oxford Dictionary of Sports Science & Medicine (3 Ed.), 3, Oxford University Press, 2007.
[51] W.G. Lindsley, T.A. Pearce, J.B. Hudnall, K.A. Davis, S.M. Davis, M.A. Fisher, R. Khakoo, J.E. Palmer, K.E. Clark, I. Celik, C. Coffey, F.M. Blachere, D.A. Beezhold, Quantity and size distribution of cough-generated aerosol particles produced by influenza patients during and after illness, J. Occup. Environ. Hyg. 9 (7) (2012) 443–449.
[52] H. Holmgren, On the Formation and Physical Behaviour of Exhaled Particles, (Ph.D. thesis), Chalmers University of Technology, SE-412 96 Goeteborg, Sweden, 2011.
[53] H. Zhang, D. Li, L. Xie, Y. Xiao, Documentary research of human respiratory droplet characteristics, in: Procedia Engineering (Ed.), 9th International Symposium on Heating, Ventilation and Air Conditioning (ISHVAC) and the 3rd International Conference on Building Energy and Environment (COBEE), Vol. 121, 2015, pp. 1365–1374.
[54] J.P. Duguid, The numbers and the sites of origin of the droplets expelled during expiratory activities, Edinb. Med. J. 52 (1945) 385–401.
[55] C.Y.H. Chao, et al., Characterization of expiration air jets and droplet size distributionsimmediately at the mouth opening, Aerosol Sci. 40 (2009) 122–133.
[56] Z. Zhang, C. Kleinstreuer, Laminar-to-turbulent fluid–nanoparticle dynamics simulations: Model comparisons and nanoparticle-deposition applications, Int. J. Numer. Methods Biomed. Eng. 27 (2011) 1930–1950.
[57] OpenFOAM The OpenFOAM Foundation, OpenFOAM foundation repository for OpenFOAM version 7, 2020, URL https://github.com/OpenFOAM/OpenFOAM-7, Accessed 18 Nov 2020.
[58] H.G. Weller, G. Tabor, H. Jasak, C. Fureby, A tensorial approach to computational continuum mechanics using object orientated techniques, Comput. Phys. 12 (1998) 620–631, http://dx.doi.org/10.1063/1.168744.
[59] J.H. Ferziger, M. Perić, Numerische Strömungsmechanik, Springer, Berlin, Heidelberg, 2008.
[60] M. Strelets, Detached eddy simulation of massively separated flows, 2001, http://dx.doi.org/10.2514/6.2001-879.
[61] Y. Tang, B. Guo, Computational fluid dynamics simulation of aerosol transport and deposition, Front. Environ. Sci. Eng. China 5 (2011) 362–377, http://dx.doi.org/10.1007/s11783-011-0365-8.
[62] F. Greifzu, C. Kratzsch, T. Forgber, F. Lindner, R. Schwarze, Assessment of particle-tracking models for dispersed particle-laden flows implemented in OpenFOAM and ANSYS FLUENT, Eng. Appl. Comput. Fluid Mech. 10 (1) (2016) 30–43.
[63] M.R. Maxey, J.J. Riley, Equation of motion for a small rigid sphere in a nonuniform flow, Phys. Fluids 26 (4) (1983) 883–889, http://dx.doi.org/10.1063/1.864230, arXiv:https://aip.scitation.org/doi/pdf/10.1063/1.864230, URL https://aip.scitation.org/doi/abs/10.1063/1.864230.
[64] C.T. Crowe, J.D. Schwarzkopf, M. Sommerfeld, Y. Tsuji, Multiphase Flows with Droplets and Particles, CRC Press, Boca Raton London New York, 2008.
[65] M. Knudsen, S. Weber, Luftwiderstand gegen die langsame bewegung kleiner kugeln, Ann. Phys. 341 (15) (1911) 981–994.
[66] D. Rader, Momentum slip correction factor for small particles in nine common gases, J. Aerosol Sci. 21 (2) (1990) 161–168.
[67] X. Jundi, Modification of stochastic model in Lagrangian tracking method, in: CFD with OpenSource Software, 2016, Edited by Nilsson H., http://www.tfd.chalmers.se/~hani/kurser/OS_CFD_2016/JundiXu/Jundi_Xu_Report.pdf.
[68] S. Balachandar, S. Zaleski, A. Soldati, G. Ahmadi, L. Bourouiba, Host-to-host airborne transmission as a multiphase flow problem for science-based social distance guidelines, Int. J. Multiph. Flow. 132 (2020) 103439, http://dx.doi.org/10.1016/j.ijmultiphaseflow.2020.103439.
[69] F.R. Menter, Two-equation eddy-viscosity turbulence models for engineering applications, AIAA J. 32 (1994) 1598–1605.
[70] J. Jeong, F. Hussain, On the identification of a vortex, J. Fluid Mech. 285 (1995) 69–94, http://dx.doi.org/10.1017/S0022112095000462.
[71] L. Schiller, A. Naumann, A drag coefficient correlation, VDI Z. 77 (1935) 318–320.
[72] E.S. Savela, A.V. Winnett, A.E. Romano, M.K. Porter, N. Shelby, R. Akana, J. Ji, M.M. Cooper, N.W. Schlenker, J.A. Reyes, A.M. Carter, J.T. Barlow, C. Tognazzini, M. Feaster, Y.-Y. Goh, R.F. Ismagilov, D.J. Diekema, Quantitative SARS-CoV-2 viral-load curves in paired saliva samples and nasal swabs inform appropriate respiratory sampling site and analytical test sensitivity required for earliest viral detection, J. Clin. Microbiol. 60 (2) (2022) e01785–21, http://dx.doi.org/10.1128/jcm.01785-21, arXiv:https://journals.asm.org/doi/pdf/10.1128/jcm.01785-21, URL https://journals.asm.org/doi/abs/10.1128/jcm.01785-21.
[73] J. Yoon, J. Yoon, J. Song, S.-Y. Yoon, C.-S. Lim, H. Seong, J. Noh, W. Kim, Clinical significance of a high SARS-CoV-2 viral load in the saliva, J. Korean Med. Sci. 35 (2020) http://dx.doi.org/10.3346/jkms.2020.35.e195.
[74] N. Mina, Breathing of Humans and its Simulation (Master's thesis), LSTM-Erlangen, Institute of Fluid Mechanics, Friedlich-Alexander-University Erlangen-Nürnberg, Cauerstr.4, D-91058 Erlangen, 2004.